Tampere University

MIKA-MATTI LAURILA

High-Precision Digital Printing Processes for Electronics Fabrication

Tampere University Dissertations 117

Tampere University Dissertations 117

MIKA-MATTI LAURILA

High-Precision Digital Printing Processes for Electronics Fabrication

ACADEMIC DISSERTATION
To be presented, with the permission of
the Faculty of Information Technology and Communication Sciences
of Tampere University,
for public discussion in the Auditorium FA032
of the Festia Building, Korkeakoulunkatu 8, Tampere,
on 13.9.2019, at 12 o'clock.

ACADEMIC DISSERTATION
Tampere University, Faculty of Information Technology and Communication Sciences
Finland

Responsible supervisor and Custos	Professor Matti Mäntysalo Tampere University Finland	
Pre-examiners	Professor Ronald Österbacka Åbo Akademi Finland	Docent Zhibin Zhang Uppsala University Sweden
Opponents	Professor Mark D. Poliks Binghamton University USA	

The originality of this thesis has been checked using the Turnitin OriginalityCheck service.

Cover design: Roihu Inc.

ISBN 978-952-03-1218-3 (print)
ISBN 978-952-03-1219-0 (pdf)
ISSN 2489-9860 (print)
ISSN 2490-0028 (pdf)
http://urn.fi/URN:ISBN:978-952-03-1219-0

PunaMusta Oy – Yliopistopaino
Tampere 2019

Abstract

This thesis investigates the capabilities of high-precision digital printing technologies in the fabrication of miniaturized components for electronics packaging, transistor interconnects and monolithically integrated lab-on-skin systems for biosignal monitoring. In general, the printing technologies suffer from poor resolution compared to conventional lithographic fabrication methods, which limits the level of miniaturization for printed electronics components, devices, and circuits. This leads to their significantly lower performance compared to conventional electronics. However, certain application areas exist where pushing the envelope of printing technologies towards higher resolution and precision would result in the addition of new functionalities.

Replacing lithographic fabrication of high-density circuitries of electronics packages with high-resolution electrohydrodynamic inkjet (E-jet) printing could result in higher levels of customizability and reduced environmental impacts. In this thesis, the parameters affecting E-jet printing resolution were studied using statistical tools; the resulting regression model applied for droplet diameters of 3.5 µm to 20 µm and had a coefficient of determination (R^2) of 94 % with a residual of 1.1 µm. Finally, the combination of E-jet and inkjet printing is demonstrated in the fabrication of a high-density (5/5 µm width/spacing) multilayer redistribution layer (RDL) for a silicon interposer.

E-jet printing could be also used to enhance the interconnect density, and concomitant performance of application specific printed electronic circuits (ASPEC), which in themselves are already an enhancement of the existing application specific integrated circuits (ASIC) in that they allow field configurability of the prefabricated logic circuits. In this thesis, E-jet printing was compared to aerosol jet (AJ), piezoelectric inkjet and lithographic fabrication methods for the fabrication of ASPECs. Two different interconnect structures were used and in both cases the E-jet printing compared favourably to AJ and piezoelectric inkjet printing technologies.

Piezoelectric inkjet printing cannot be considered a true high-resolution technology similar to E-jet printing due to its large droplet volume (pL vs. fL), However, it may still be used to print small (i.e., *high-precision*) structures required for example in transistor fabrication. The high-precision printing capability coupled with a large droplet volume enables higher throughput when fabricating amplifiers with monolithically integrated active and passive components. In this thesis, a piezoelectric inkjet was used for the fabrication of source/drain (S/D) electrodes for transistors with ~10 µm channel length together with monolithically integrated large area parallel plate capacitors and resistors. The resulting charge amplifier optimized for pulse wave (PW) measurements had a gain of 1.6 V/nC

with a pass band of 50 MHz to 32 Hz. Furthermore, the performance of the amplifier was evaluated for PW measurements by amplifying a PW signal recorded using piezoelectric poly(vinylidene-trifluoroethylene) (P(VDF-TrFE) pressure from the radial artery at the wrist and analyzing the amplified signal for clinically relevant PW features. As a supporting study, the PW signal generated by a fully printed P(VDF-TrFE) pressure sensor was evaluated in a pre-clinical study with a statistically significant number of study subjects (22). Clinically relevant indices were calculated from the PW signal generated by the P(VDF-TrFE) sensor and these were compared to concurrent measurement with a reference PW sensor. Good agreement between the PW sensors could be found in the case of the stiffness index (SI) and radial augmentation index (rAIx).

.

Preface

The work related to this thesis was done by the Printed Electronics Research Group at Tampere University, Finland, from 2016 to 2019.

This thesis was made possible by ENIAC-JU/Tekes funded Prominent, Tekes funded Naked Approach, and Academy of Finland funded Vascular Biomechanics Assessment projects. I also wish to acknowledge the Tuula and Yrjö Neuvo Foundation and Electronic Engineers Foundation for their generous personal grants and TU Dresden for the research exchange grant.

As for the non-financial support, I would first and foremost like to express my gratitude to my supervisor Prof. Matti Mäntysalo for his guidance and support throughout the thesis work. I also wish to thank Dist. Prof. Shizuo Tokito at the Tokito-Kumaki-Sekine Laboratory (Yamagata University, Japan) and Prof. Karl-Heinz Bock at the Institute of Electronic Packaging Technology (Institut für Aufbau und Verbindungstechnik, TU Dresden, Germany) for letting me benefit from their expertise and infrastructure. Many thanks also go to all the co-, main- and co-main-authors, especially the following: Prof. Niku Oksala, Assoc. Prof. Hiroyuki Matsui, Assist. Prof Antti Vehkaoja, Assist. Prof. Tomohito Sekine, as well as Mohammad Mashayekhi, Ph.D. and Mikko Peltokangas, M.Sc.. I also wish to express my gratitude to the current and former colleagues at the Laboratory of Future Electronics, especially: Behnam Khorramdel, D.Sc., Assist. Prof. Jiantong Li, Tiina Vuorinen, M.Sc., Riikka Mikkonen, M.Sc., Milad Mosallaei, M.Sc., Anna Railanmaa, M.Sc., Miao Li, M.Sc., Jari Keskinen, D.Sc., Martin Schubert, M.Sc., Sebastian Lüngen, M.Sc. and last (but definitely not least) Karem Lozano Montero, B.Sc. Thank you for all the helpful and not-so-helpful conversations, which, somehow, ended up helping the most.

During the studies, I also had the opportunity to escape the Hervanta-Jämijärvi-Pori triangle and there I met some great people worth a mention: Varvara Salonikidou, M.Sc. (Barbara-san), Basanagouda Patil, M.Sc. (Basu-san), Taisei Mano, M.Sc., and Hiroyuki Nakamura, M.Sc. “Arigatõ” very much!

…and of course, this whole thing would not be possible without the family and friends. Et tattist vaa teillekki!

Tampere 30.04.2019

Author

Contents

List of Figures

List of Tables

List of Symbols and Abbreviations

2.5D	Two and half dimensional
3D	Three dimensional
Ag	Silver
AJ	Aerosol jet
ANOVA	Analysis of variance
ASIC	Application specific integrated circuit
ASPEC	Application specific printed electronic circuit
Au	Gold
CMOS	Complementary metal oxide
CTE	Coefficient of thermal expansion
CV	Coefficient of variation
CVD	Cardiovascular disease
d_{33}	Piezoelectric coefficient
DMP	Dimatix material printer
DoD	Drop-on-demand
DOE	Design of experiments
E-jet	Electrohydrodynamic inkjet
EMFi	Electromechanical film
EMI	Electromagnetic interference
f_t	Transition frequency of field effect transistor
γ_{LV}	Surface energy of the liquid-vapor interface
γ_{SL}	Surface energy of the solid-liquid interface
γ_{SV}	Surface energy of the solid-vapor interface
IC	Integrated circuit
IJ	Piezoelectric inkjet

I/O	Input/output
L	Channel length
MEMS	Microelectrocmechanical system
MET	Metallization layer
MIM	Metal-insulator-metal
MOD	Metal organic decomposition
μ_s	Semiconductor mobility
OTFT	Organic thin film transistor
PW	Pulse wave
R^2	Coefficient of determination
rAIx	Radial augmentation index
RDL	Redistribution layer
RI	Reflection index
PEDOT:PSS	Poly(3,4-ethylenedioxythiophene):poly(styrenesulfonate)
PET	Poly(ethylene terephthalate)
PCB	Printed circuit board
P(VDF)	Poly(vinylindenefluoride)
P(VDF-TRFE)	Poly(vinylindenefluoride-trifluoroethylene)
PZT	Lead zirconate titanate
RF	Radio frequency
S/D	Source/drain
SI	Stiffness index
SIJ	Super Inkjet
SiO2	Silicon dioxide
SIP	System-in-package
θ	Contact angle
Ti	Titanium

TSV	Through silicon via
UBM	Under bump metallization
UV	Ultraviolet
V_{GS}	Gate-to-source voltage
V_{TH}	Threshold voltage
VTC	Voltage transfer characteristic
W	Tungsten
W/S	Width/spacing
wt%	Weight percentage

List of Publications

I. **Laurila M. M**., Khorramdel B., Dastpak A., Mäntysalo M. “Statistical Analysis of E-jet Print Parameter Effects on Ag-nanoparticle Ink Droplet Size”, Journal of Micromechanics and Microengineering, 27(2017)9, p. 095005

II. **Laurila M.-M**, Khorramdel B., Mäntysalo M., ”Combination of E-jet and Inkjet Printing for Additive Fabrication of Multilayer High-Density RDL of Silicon Interposer, IEEE Transactions on Electron Devices, 64(2017)3, pp. 1217-1224

III. Mashayekhi M., Winchester L., Louise E., Pease T., **Laurila M.-M.,** Mäntysalo M., Ogier S., Teres L., Carrabina J., “Evaluation of Aerosol, Superfine Inkjet and Photolithography Printing Techniques for Metallization of Application Specific Printed Electronic Circuits”, IEEE Transactions on Electron Devices, 63(2016)3, pp. 1246-1253

IV. Mashayekhi M., Winchester L., **Laurila M.-M.,** Mäntysalo M., Ogier S., Teres L., Carrabina J., “Chip-by-Chip Configurable Interconnection Using Digital Printing Techniques”, Journal of Micromechanics and Microengineering, 27(2017), p. 0450009

V. **Laurila M.-M.,** Matsui M., Shiwaku R., Peltokangas M., Verho J., Montero L. K., Sekine T., Vehkaoja A., Oksala N., Tokito S., Mäntysalo M., ”A Fully Printed Ultra-Thin Charge Amplifier for On-Skin Biosignal Measurements”, Journal of Electron Device Society, 7(2019), pp. 566-574

VI. **Laurila M.-M.,** Peltokangas M., Montero K. M., Honkanen M., Siponkoski T., Juuti J., Tuukkanen S., Oksala N., Vehkaoja A., Mäntysalo M., ”Evaluation of Printed P(VDF-TrFE) Pressure Sensor Signal Quality in Arterial Pulse Wave Measurement”, IEEE Sensor Journal, Accepted for publication, DOI: 10.1109/JSEN.2019.2934943

1 Introduction

The miniaturization of electronic devices has been one of the major drivers behind the universal adoption of electronic equipment in our every-day life. The most prominent success of this paradigm has been the fabrication of current hand-held, portable computers that far outperform the table-top computers of 20 years ago. One could therefore argue that the increased operating speed of the electronic devices is as important as the device miniaturization. However, even the well-known Moore's law is in fact a law of miniaturization (instead of processing speed), because it states that the transistor density on integrated circuit (IC) chips will double every 18 months [1]. The success of Moore's law in predicting the increase in operating speed is based on the *miniaturization* of transistors. This leads to faster switching speeds according to Dennard scaling [2], and the ability to fabricate complex circuits through monolithic integration of active and passive devices on the same semiconductor chip (Kilby's invention [3]), which enables faster communication between the devices. Another form of miniaturization has taken place on a higher electronics packaging level where more functionalities have been incorporated in the same package, such as in the case of monolithic integration of microelectromechanical system (MEMS) transducers and processing circuits on the same chip [4]. This has reduced the number of required packages on printed circuit boards (PCB) and also increased the operating speeds due to shorter signal paths between devices inside the package [4]. At the moment, the majority of electronic component fabrication processes employ tools which are based on subtracting (i.e., etching) material to form electrically functional features. These subtractive fabrication methods are highly advanced and are able to produce horizontal features at a resolution of 14 nanometres [5], or few hundred atoms, and vertical features at resolutions of approximately one nanometre [6], or a few atoms. However, they also suffer from drawbacks such as complicated, multi-step process flows, large amounts of waste materials and the use of hazardous etching chemicals.

These drawbacks have produced the on-going paradigm shift in electronic fabrication towards more environmentally friendly additive fabrication methods, colloquially known as printed electronics.

These methods selectively deposit solution processable materials in the required areas followed by suitable post-processing steps (e.g., curing or sintering) [7]. This process is then repeated until the complete device has been built on the substrate. In addition to the obvious material saving potential, additive fabrication methods also reduce the processing temperature, number of required process steps, and simplify the fabrication process to enable more flexible process flows. Especially, digital printing technologies (e.g., inkjet and electrohydrodynamic jet printing) offer highly customizable process flows by using digital printing files instead of physical masks. However, because the majority of the printed electronics fabrication tools have been adapted from graphic art processes (e.g., screen, gravure, flexography, and inkjet printing), they also suffer from the same drawbacks. The most notable of these are their limited resolution [8]. At best, digital printing tools are able to produce features on a scale of a few micrometres, or three orders of magnitude more than the aforementioned subtractive methods. It is therefore important to investigate how to increase the resolution and reduce the critical feature size in order to enable the miniaturization, and wider adoption, of *printed* electronics devices.

1.1 Aim and scope of the thesis

This thesis investigates the capabilities and limitations of three high-precision digital printing technologies, the piezoelectric inkjet, electrohydrodynamic inkjet, and aerosol jet printing. The term high-precision is used here to include both high resolution *and* fine feature sizes, both of which are required to fabricate miniaturized components and increase their operating speed.

First the printing parameters affecting the resolution of the electrohydrodynamic inkjet (E-jet) printer are studied. This is followed by comparison of piezoelectric inkjet, aerosol and E-jet printing quality (especially the resolution) for interconnected fabrication for application-specific printed electronic circuits (ASPEC), and a demonstration of E-jet/piezoelectric inkjet printed high-density (5/5µm W/S) redistribution layers in electronics packaging applications. The high-precision printing capability of the piezoelectric inkjet printer is demonstrated in the fabrication of a charge amplifier with monolithically integrated passive components; the reproducible fabrication of source/drain electrodes for organic transistors with a length less than 10 µm is demonstrated. Finally, a piezoelectric sensor system with piezoelectric inkjet printed bottom electrode is demonstrated.

1.2 Structure of the thesis

This thesis is divided into three chapters and a conclusion. The first chapter introduces the topic of the thesis followed by a short discussion on its aims and scope and concludes with the authors contributions to the publications presented at the end of the thesis. The second chapter discusses

the fundamentals of high-precision patterning in printed electronics and presents the three main printing technologies, piezoelectric inkjet, electrohydrodynamic inkjet and aerosol jet printing, employed in the publications. The third chapter introduces the three different printed electronics applications where high-precision patterning is required and also discusses and expands upon the research results of the publications.

1.3 The author's contribution

Publication I. The author was the main contributor, designed the experiments, fabricated and measured the test structures, analyzed the data and wrote the manuscript. B. Khorramdel and A. Dastpak helped to carry out the measurement system analysis. M. Mäntysalo revised and improved the manuscript.

Publication II. The author was a co-contributor and designed the print files, optimized the process, fabricated the test structures, analyzed the results, and wrote a chapter in the manuscript regarding E-jet printing. The chapter was then revised and improved by other co-authors.

Publication III. The author was a co-contributor and designed the print files, fabricated the test structures and wrote a chapter in the manuscript regarding E-jet printing. The chapter was then revised and improved by other co-authors.

Publication IV. The author was the main contributor and designed, fabricated and measured the test structures, analyzed the data and wrote the manuscript. B. Khorramdel did the SEM imaging and analysis. M. Mäntysalo revised and improved the manuscript.

Publication V. The author was the main contributor and designed, fabricated and measured the test structures, analyzed the data and wrote most parts of the manuscript. H. Matsui designed the charge amplifier and wrote the amplifier design paragraph; R. Shiwaku helped with the fabrication of the test structures; M. Peltokangas did the arterial pulse wave measurements, analyzed the data and wrote the respective paragraph; J. Verho designed and implemented the buffer amplifier and K. Lozano Montero fabricated the P(VDF-TrFE) pulse wave sensors. The manuscript was revised and improved by other co-authors.

Publication VI. The author shared the main contribution with M. Peltokangas. He developed the fabrication process and designed the P(VDF-TrFE) pulse wave sensors, which he also helped to fabricate and characterize, and wrote most parts of the manuscript. M. Peltokangas measured and analyzed the arterial pulse wave signals and wrote the respective paragraphs; K. Lozano Montero fabricated the P(VDF-TrFE) pulse wave sensors; T. Siponkoski took the polarization-electric field hysteresis loop measurements. The manuscript was revised and improved by other co-authors.

2 Digital high-precision printing techniques

Printed electronics employs solvent based materials (i.e., solutions or dispersions), generally referred to as *inks*, to make electrically functional features which may be either conducting, semi-conducting or dielectric. Using materials with these three properties, it is possible to fabricate conductors [9], inductors [10], resistors [11], capacitors [10], transistors [12], diodes [13] and different types of transducers [14] required to make any form of electronic equipment. In order to achieve the required electrical functionality, the material properties have to be chosen to suit the application: for example, an organic light emitting diode requires a specific type of semi-conducting material (i.e., a direct band-gap semiconductor) compared to a simple diode and a piezoelectric sensor requires a specific type of dielectric (i.e., a ferroelectric dielectric) compared to a simple capacitor. Secondly, a suitable ink formulation must be found because the ink rheology (e.g., the viscosity and surface tension) and other physical properties (e.g., the solvent vapour pressure and particle size) affect the quality of the deposited film. Fortunately, the ink formulation problem has been solved for most material types so that there are several commercially available inks customized for different printing tools. Thirdly, a suitable printing tool must be chosen. The most notable differences in printing tool characteristics are related to their resolution and throughput (see Table 1), while the direct deposition drop-on-demand technologies (e.g., piezoelectric inkjet and E-jet printing) offer additional benefits of having highly customizable process flows due to their use of digital print files instead of physical print rolls or masks [15], [22]. Although the resolution of the piezoelectric inkjet is limited to 30-50 µm, it has a high droplet position accuracy of 5 µm, which enables high precision patterning required in certain applications (e.g., transistor channel lengths). The E-jet printing is also suited for high-density circuits, where a small line width is important. Together these two printing methods can therefore be termed “digital high-precision printing techniques”.

The motivation of this chapter is to understand the capabilities these high-precision digital printing technologies have for fabrication of miniaturized printed electronics devices discussed in Chapter 3. First, the functioning principles of the printing methods are explained focusing on parameters which affect their high precision pattern formation (e.g., positioning accuracy, droplet size etc.) and followed

by a comparison of their benefits/advantages. This is followed by introduction of the term “high precision pattern formation” through the concepts of resolution and droplet wetting on the substrate surface. In addition, the parameters affecting the line width and edge/surface roughness are explained because they are important for creating uniform features without unwanted open or short circuits that could lead to defects in highly miniaturized devices.

Table 1: Comparison of different printing technologies. Adapted from [8].

Printing method	Line width (µm)	Line thickness (µm)	Printing speed (m/min)	Print file type
Piezoelectric inkjet	30-50	0.1-1	1-500	Digital
Electrohydrodynamic inkjet	1	0.001-0.1	<1	Digital
Dispensing	10-1000	50-100	Single stroke	Digital
Offset	10	1-10	1000	Physical
Gravure	10-50	0.1-1	1000	Physical
Flexo	45-100	<1	500	Physical
Screen	30-50	5-100	30-150	Physical
Gravure offset	5-20	1-3	1-10	Physical
Reverse offset	1-10	0.05-1	0.01	Physical
Nanoimprinting	-	0.01	0.1	Physical

2.1 Piezoelectric inkjet printing

Most inkjet printers used in the additive fabrication of electronic devices are of the drop-on-demand (DoD) type. The operation of a DoD inkjet printer is based on the ejection of single droplets from a print head containing tens or hundreds of nozzles. By accurately controlling the timing and position of the ejection from each individual nozzle, complicated patterns can be formed on the substrate. This allows the use of digital print files and rapid changes in the printed pattern resulting in a highly customizable fabrication process [15].

The predominant droplet ejection mechanism of the DoD printers used in printed electronics fabrication is based on piezoelectric actuation. The upper part in Figure 1 shows the simplified structure of a single piezoelectrically actuated nozzle, while the lower part shows the time series leading to droplet formation. The ink is fed into the ink chamber from the ink supply channel via a connecting channel. The piezoelectric element, commonly made of lead zirconate titanate (PZT), is situated next to the ink chamber behind a flexible wall and the ink chamber is connected to the environment via a nozzle situated opposite the connecting channel. During droplet formation, a voltage signal is fed to the piezoelectric element causing it to bend. When the bending motion is towards the ink chamber, the chamber volume contracts and a positive pressure wave moves towards the nozzle. If the energy imparted by the pressure wave on the ink meniscus on the nozzle is large enough, the meniscus starts to elongate until the elongated ink ligament is thin enough for the surface tension of the ink pinch off. The leftover ligament contracts towards the main droplet during the droplet flight from the nozzle to the substrate. Depending on the velocity of the ejected droplet and the ink parameters (e.g., surface tension and viscosity), the ligament may not be able to contract fully before a secondary pinch off occurs and generates a secondary (or satellite) droplet which is smaller than the main droplet. This often forms a print defect because the position of the satellite droplet will be somewhat offset from the intended position of the main droplet on the substrate, thus causing an increase in the edge roughness of the printed line [15].

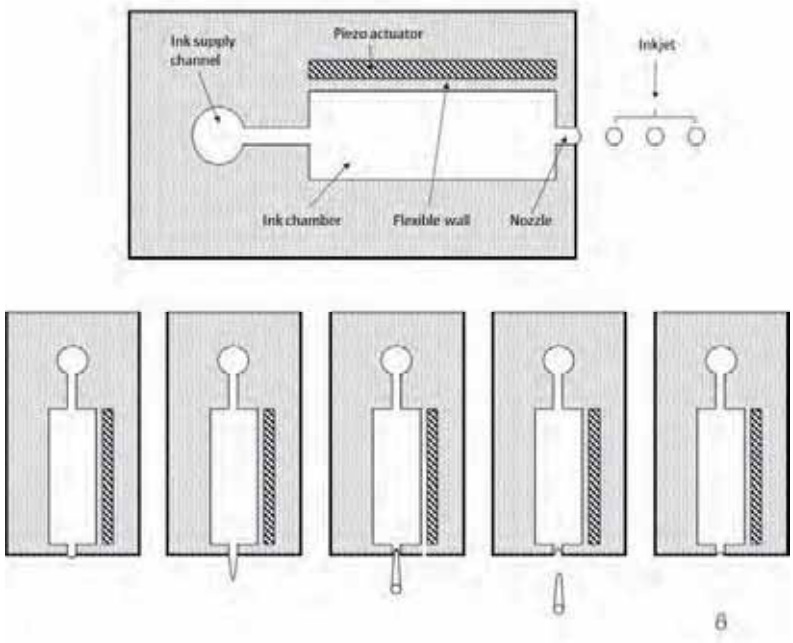

Figure 1: Operation principle of a piezoelectric inkjet printer. Adapted from [15].

The droplet size of the DoD printers utilizing the piezoelectric actuation mechanism is mainly defined by the diameter of the nozzle, while the voltage signal pulse wave form and amplitude may have a small effect as well. The spreading of the droplet on the substrate is affected by the substrate surface energy, ink surface tension and droplet volume (discussed more thoroughly in Chapter 2.3). For example, the print heads compatible with the DMP-2800 utilized in this thesis (see Figure 2) are offered in 1 pL or 10 pL sizes, which result in a minimum of a 30-50 µm line width on the substrate once the substrate surface energy has been optimized [15].

The droplet positioning accuracy of the DoD inkjet printer is system specific and errors may be caused by an error in the movement of the print head and the print stage and errors in the droplet ejection direction, which is also proportional to the print height [16]. For most commercial inkjet inks, the ink formulation is optimized so that the droplet-to-droplet variation in the ejection direction is minimal. For the DMP-2800 the droplet positioning accuracy is +/- 5 µm including both the print head movement and stage movement errors. From the high precision printing point of view this means that the smallest feature sizes which can be printed using the DMP-2800 are in the order 10 µm and are therefore significantly smaller than its minimum line width of 30-50 µm. This type of fine feature printing can be utilized in applications such as high-density circuitry where the 10 µm spacing between adjacent conductors increases the conductor packing density (i.e., a maximum packing density of 30/10 µm W/S) when compared to screen printed structures, for example, where the resolution indicates both the line width and spacing (i.e., a maximum packing density of 40/40 µm W/S). Another important application of the fine feature patterning capability can be found in field effect transistors, where the switching speed depends on the material parameters (e.g., semiconductor mobility, gate dielectric capacitance) and their channel length (i.e., the gap between the source and drain electrodes) [17]. Since the material parameters are in most cases fixed, minimizing the channel length offers a natural way to increase transistor performance. The fine patterning capability of the DMP-2800 is utilized in **Publication V** to fabricate source and drain electrodes for organic semiconductor transistors with channel lengths of approximately 10 µm.

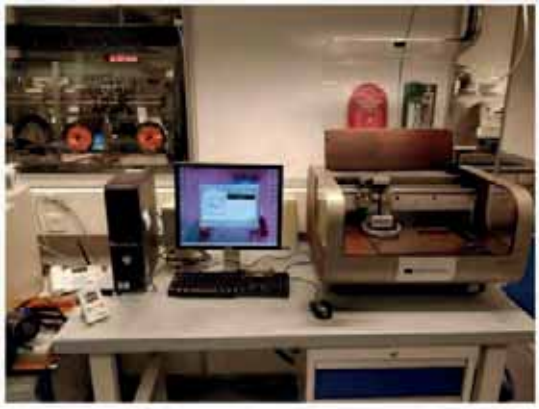

Figure 2: The DMP-2800 piezoelectric inkjet printer used in this thesis [70]

The throughput of a piezoelectric inkjet printer is determined by the number of active nozzles together with the resolution of the print file and the droplet ejection frequency. The resolution of the print file and the maximum droplet ejection frequency determine the maximum movement speed of the print head so that when the print file resolution is increased, the printing speed is decreased. This can be combated by increasing the number of active nozzles: for example, industrial scale printers can be fitted with print heads with multiple thousands of nozzles (e.g., the 2,048 nozzle Samba GL3 printhead [18]) which enable comparable throughput to offset type roll-to-roll and screen printing methods [8]. Furthermore, because piezoelectric inkjet printers use digital print files, the exchange-of-die times are very short. This leads to significantly faster prototyping and small-batch fabrication when compared to roll-to-roll/screen printing technologies utilizing physical print masks. When compared to the higher resolution E-jet technology (discussed more thoroughly in the next chapter), the throughput of the piezoelectric inkjet printer compares favourably due to the lower maximum droplet ejection frequency and smaller droplet size of the E-jet printers. This becomes especially apparent when the print file includes both large *and* fine features, such as the one square millimeter parallel plate capacitor electrodes and short channel transistors demonstrated in **Publication V**.

2.2 Electrohydrodynamic inkjet (E-jet) printing

Unlike most printed electronics fabrication tools, the electrohydrodynamic inkjet (E-jet) printer was derived from electrospray devices used for atomization of liquids instead of equipment used in graphic printing. The main benefit of this technology is the generation of very small volume droplets, which are able to increase the resolution 30 to 50-fold compared to piezoelectric inkjet printers, while still using digital print files to achieve a highly customizable process. Previously, E-jet technology

has been used, for example, in the fabrication of high-resolution S/D contacts for transistors [19], 3D microstructures with phase change inks [20] and transparent Ag-nanowire electrodes [21], [22].

The operating principle of the E-jet printer is shown in the upper part of Figure 3 and the droplet ejection mechanism in the lower part. During operation the ink (3) inside the ink chamber (1) is charged using a charging electrode (2), which is controlled by computer (5) via a wave form generator (6) and high voltage amplifier (7). The droplet ejection mechanism is based on the force balance between the hydrostatic force which supplies ink to the meniscus, the surface tension which keeps the meniscus attached to the nozzle and an electrostatic force which pulls the meniscus downwards [23]. When the electric field between the meniscus and the print stage (9) exceeds a threshold value, this force balance is disrupted, and droplet ejection occurs. The main benefit of this type of droplet ejection mechanism is that it is able to generate droplets with a smaller diameter than the nozzle and that the droplet volume can be varied to a higher extent compared to the pressure-wave-based ejection mechanism of piezoelectric inkjet printers. However, there are multiple parameters affecting the volume of the ejected droplets and understanding these is important for repeatable and reproducible high-resolution patterning with E-jet printer.

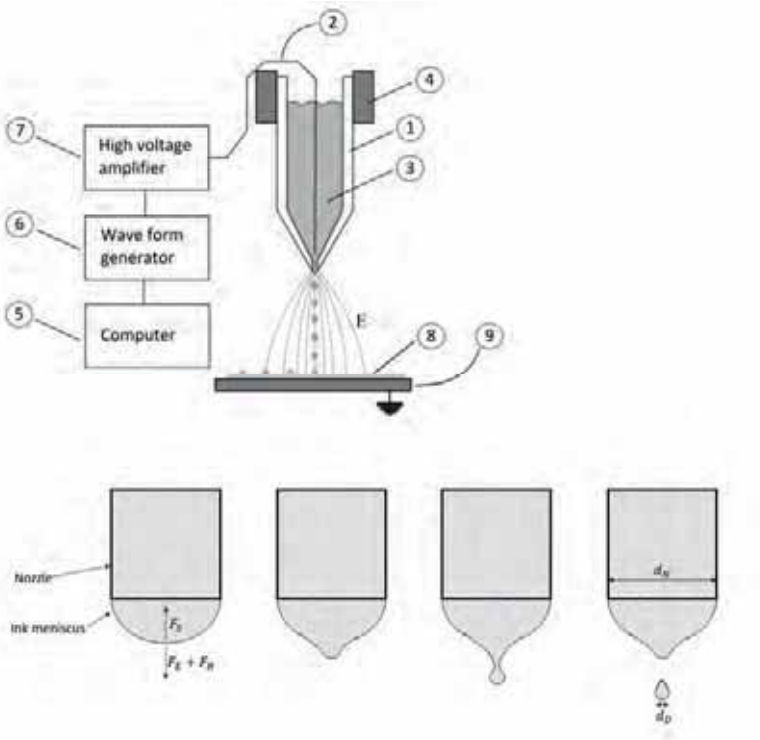

Figure 3: The operating principle of an E-jet printer (upper part, [24]) and the time series leading to droplet ejection (lower part).

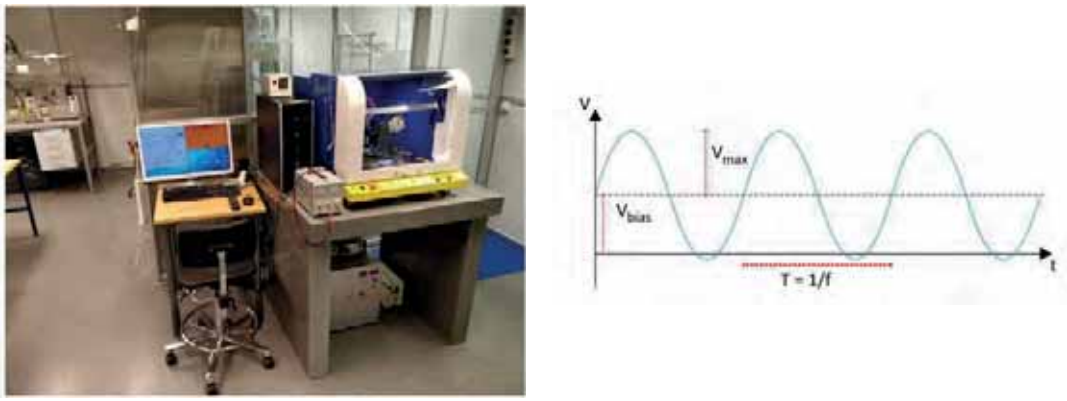

Figure 4: The E-jet printer used in this thesis (left) and the voltage waveform for droplet ejection used in **Publications I, II, III, IV** (right, [24]).

In **Publication I,** a statistical analysis of the print parameter effects on the droplet volume was carried out for a commercial E-jet printer, the Super Inkjet (Figure 4 a). In this study, a design of experiments (DoE) methodology was used with an analysis of variance (ANOVA) to relate four print parameters (nozzle-to-substrate height, bias voltage, amplitude and frequency) to the deposited droplet width.

In this study, a commercial conductive inkjet ink consisting of Ag-nanoparticles dispersed in triethylene glycol monoethyl ether solvent at a weight percent of 30-35 % (DGP 40TE-20C, by Advanced Nano Products) was used together with a silicon wafer substrate coated with conductive titanium-tungsten (Ti/W). An electrical connection between the Ti/W surface and grounded print stage was made in order to further ensure that there was no charge accumulation on the substrate during printing. Environmental parameters such as the humidity and temperature were controlled during the experiments.

A DoE utilising response surface design was chosen to include possible quadratic effects in the model. A response surface regression model based on the ANOVA results was applied for droplet diameters between 3.5 to 21 µm with an R-squared value of 94 % and a residual of 1.1 µm, which demonstrated the repeatable high-resolution patterning capability of the E-jet printer.

The test results indicated that the amplitude of the electric field has the strongest effect, followed by the nozzle-to-substrate print height, bias voltage and frequency. It must be noted however, that in the case of dielectric substrates, the effect of nozzle-to-substrate print height becomes more complex because the electric field generating the droplets will be between the print stage and the nozzle and the dielectric substrate permittivity, and thickness, will therefore affect the volume of the ejected droplet. It was also found that the nozzle-to-substrate height and frequency have inverse relations with the print resolution, whereas the bias voltage and amplitude have a positive relation. Thus, increasing the nozzle-to-substrate height leads to a lower electric field strength and higher print resolution. Additionally, the same effect can be achieved by lowering the bias voltage or amplitude.

However, it was also found that the higher nozzle-to-substrate distance increases the edge roughness of the deposited droplets. This indicates that varying the voltage bias or amplitude is the preferred way to achieve high-resolution printing. Another possible way to achieve high-resolution printing is to increase the frequency because this reduces the voltage pulse width, which has an inverse proportion to the ejected droplet volume [25]. A graphical interpretation of these results is shown in Figure 5.

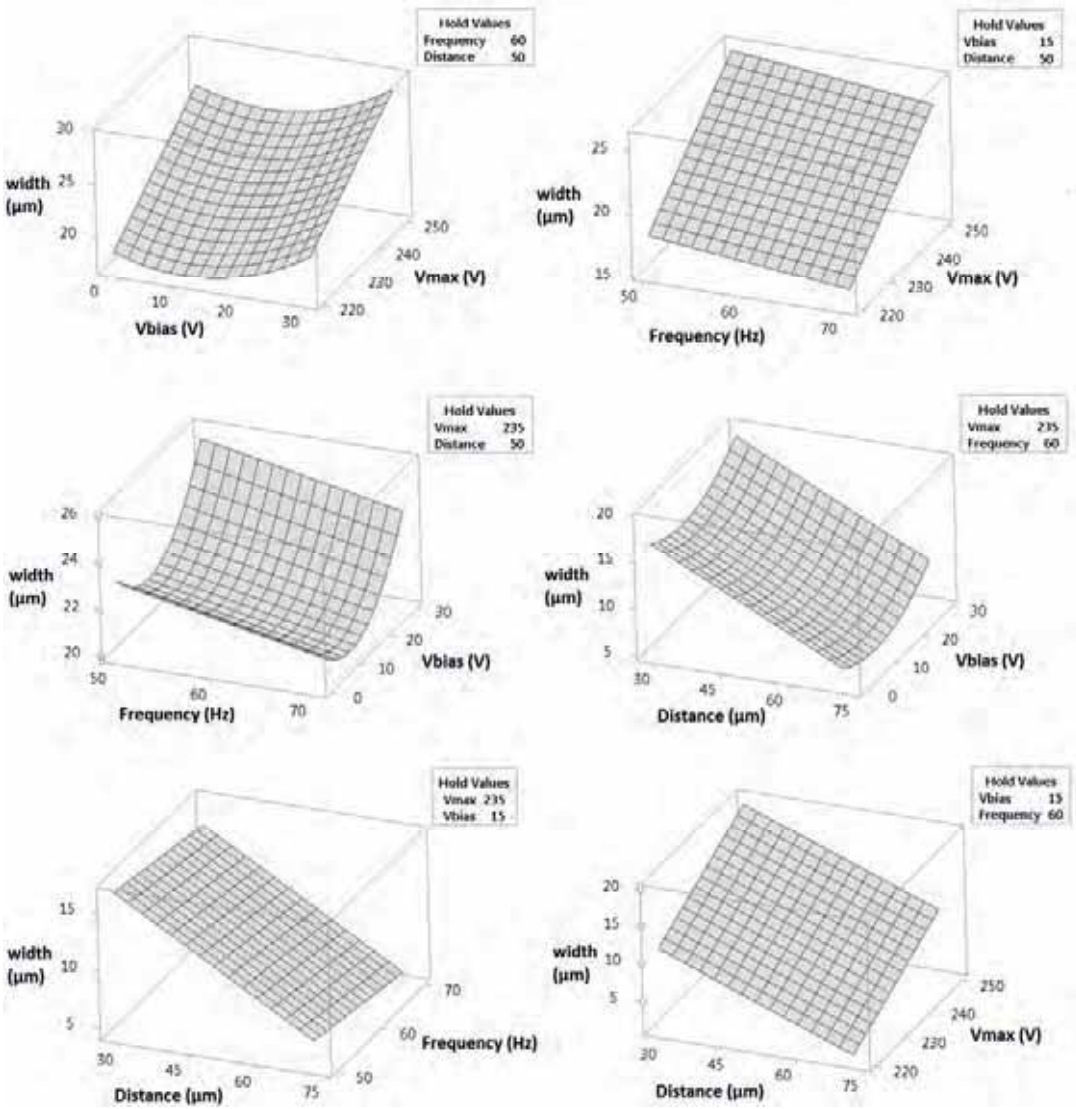

Figure 5: The effect of print parameters on the deposited droplet diameter (from **Publication I)**, © 2017 IOP Science.

Furthermore, the reproducibility of the print process was evaluated by printing confirmation runs with three additional nozzles at two different print heights (50 µm and 70 µm). A lower nozzle-to-substrate distance yielded more reproducible results in which all the droplets for two nozzles were within the model's 95% confidence intervals.

Thus, when utilizing an E-jet instead of a piezoelectric inkjet printer, the print resolution could be increased 10-fold with high repeatability and reproducibility. With this type of printer it would be possible to further increase the packing density of high-density circuitry to at least 5/5 µm W/S, which would be an eight-fold increase compared to the 30/10 µm W/S of the piezoelectric inkjet printer discussed in the last section. The high-density circuit printing enabled by the E-jet technology is further investigated in **Publications II, III and IV** in Chapters 3.1.and 3.2.

The main challenge of E-jet printing is the low throughput. For example, the Super Inkjet printer used in the aforemetioned studies has a maximum droplet ejection frequency of 1 kHz. The maximum printing speed for a line consisting of 5 µm diameter droplets with a 50% overlap is therefore 2.5 mm/s. However, the droplet positioning accuracy is approximately 50-fold better and the viscosity range of suitable inks is 100-fold larger compared to piezoelectric inkjet printers.

2.3 Aerosol jet printing

Similar to E-jet printing, the aerosol jet (AJ) printing is a novel high-resolution fabrication method with first commercial printers developed as late as in the beginning of this century [26][30]. Regarding interconnect fabrication, the AJ printing has been previously utilized in fabrication of 14 µm wide current collectors for photovoltaic applications [27], 10 µm wide transmission lines for 3D packaging application [28] while the process parameters affecting the high-resolution printing of 20 µm wide silver tracks have been studied by Mahajan et al. in [29].

The functioning principle of the aerosol jet is based on aerosolization of source material (i.e. electrically functional ink) inside aerosolization chamber and transfer of the aerosol from chamber to deposition head and further to substrate using an inert carrier and sheath gas. The principle of aerosolization is based either on ultrasonic or pneumatic actuation depending on the viscosity of the ink (< 5 mPa·s for the former, and 1 to 1000 mPa·s for the latter). The pneumatically actuated aerosolization is based on Collison-method (see Figure 6, left part) whereby a high velocity inert carrier gas (e.g. N2, Ar, He) is driven through a horizontal channel which is connected to ink supply by vertical channel. The high velocity carrier gas forms a low pressure region inside the vertical channel which pulls the ink upwards until it is level with the walls of the horizontal channel. Once this happens, the high velocity gas imparts high shear forces on the ink meniscus and causes droplets to form. The aerosol is then driven towards the outlet of the horizontal channel where a bifurcation point leads to the deposition head or the source material reservoir. At this point, the high inertia, large volume

droplets are driven back to source material reservoir, while the low inertia, small volume droplets are driven with the carrier gas towards the deposition head thereby reducing the size and polydispersity of the droplets. However, the aerosol still contains droplets which have too low volume and which

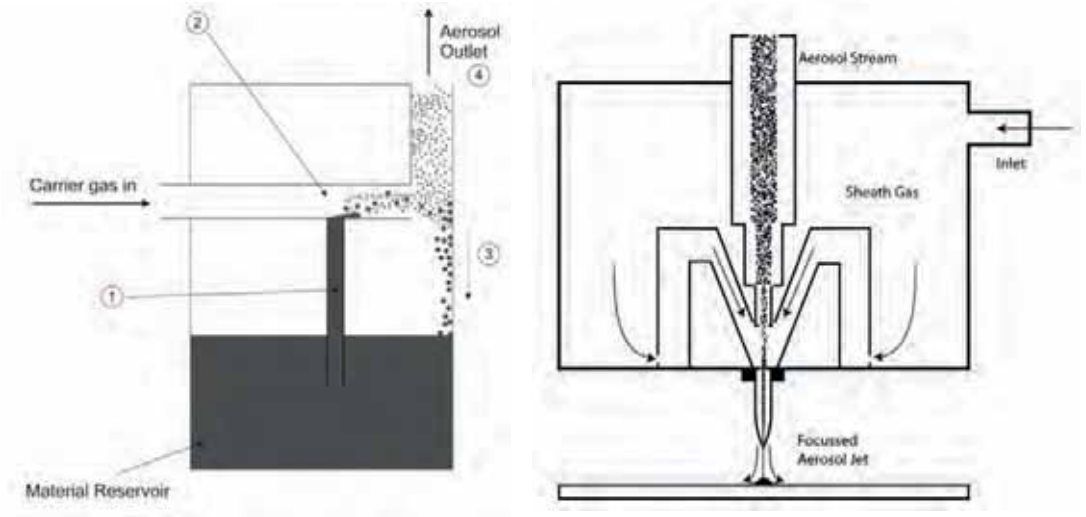

Figure 6: Aerosol jet printer pneumatic aerosolization chamber (left) and deposition head (right). © 2019 Springer.

may lead to print defects (similar to the satellite droplets in piezoelectric inkjet printer) and these need to be removed from the aerosol stream in a virtual impactor (this also removes part of the excess carrier gas to increase the aerosol concentration). [30]

The deposition head consists of a virtual nozzle, where the aerosol stream is enveloped in an inert sheath gas and constricted (see Figure 6, right part), and a physical nozzle, which further constricts the aerosol stream before deposition. The resulting aerosol stream is highly collimated, which enables the use of relatively large print heights (1 to 5 mm) without adverse effects on the print resolution, a clear advantage over the E-jet printing (print heights in the order of tens to few hundreds of µm) if the substrate has significant topography. Furthermore, the probability of nozzle clogging is reduced because the sheath gas acts as protective layer between the nozzle walls and aerosol stream. The degree of stream constriction can be varied by varying the ratio of sheath to carrier gas flow rate (i.e. the focussing ratio [29]) thereby enabling the digital control of the print resolution over large range (i.e. ~10 µm to few mm [31]). The use of sheath gas also enables the use of inks containing relatively large nanoparticles (up to 500 nm diameter [32]) when compared to inks developed for piezoelectric inkjet printing (typical diameter in 10s of nm range [50]). [30]

2.4 Comparison of piezoelectric inkjet, E-jet and aerosol jet printer

The main characteristics of the piezoelectric inkjet, E-jet and aerosol jet printer used in this thesis are summarized in the Table 2. Positioning accuracy indicates the accuracy of the droplet placement in a process run while the alignment accuracy is related to the droplet placement between process runs. The main benefits of the SIJ-S050 over the DMP-2800 and Optomec 300 are the smaller droplet volume and resolution, higher ink viscosity range and higher positioning and alignment accuracy. The main benefit of the DMP-2800 is its higher throughput due to multiple nozzles and higher printing speed. The latter is not listed in Table 2 because it depends on both the droplet ejection frequency and print file resolution.

Table 2: Characteristics of the piezoelectric inkjet (DMP-2800),E-jet (SIJ-S050) and aerosol jet printer (Optomec 300) printer utilized in this thesis [70].

	Dimatix Material Printer (DMP-2800)	Super Inkjet (SIJ-S050)	Aerosol jet (Optomec 300)
Droplet ejection mechanism	Piezoelectric	Electrohydrodynamic	Aerodynamically controlled aerosol
Ink viscosity range	2-30	0.5-10,000	0.7-1000
Droplet volume	1 pL or 10 pL	0.1 fL to 10 pL	~0.5 to ~600 fL
Number of nozzles	16	1	1
Print area (mm²)	210*315	50*50	300*300
Positioning accuracy	± 5	± 0.1	± 5
Alignment accuracy	± 25	± 0.2	± 2

2.5 High-precision pattern formation

The resolution of a printing method is defined as the smallest distance between two distinct printed patterns and it is generally expressed as the minimum line width/spacing (e.g., 5/5 µm W/S) [8]. The term “high-precision” is used here instead of “high-resolution” to include the case where the minimum spacing between the lines is significantly smaller than the line width. It is then apparent that high-

precision pattern formation is based on achieving narrow lines and/or small spacing between the lines. In DoD technologies, lines consist of overlapping single droplets and the line width is therefore affected by the spreading of the single droplet on the substrate.

2.5.1 Droplet spreading on the substrate

The spreading of a single droplet on the substrate is mainly determined by the interaction between the ink and the substrate. In the case of a smooth and chemically homogenous substrate and an ideal liquid, the spreading of the liquid (i.e., wetting) is defined by the equilibrium contact angle of the droplet at the liquid-vapor and solid-liquid interface, which can be calculated using the Young equation (also see the upper part of Figure 7):

$$\cos(\theta) = \frac{\gamma_{SV} - \gamma_{SL}}{\gamma_{LV}}$$

where θ is the contact angle, γ_{SV} is the surface energy of the solid-vapor interface, γ_{SL} is the surface energy of the solid-liquid interface and γ_{LV} is the surface energy of the liquid-vapor interface [33]. Thus, the spreading of the droplet can be adjusted by varying the relationships between the different surface energies. In practice, the surface energy of the liquid-vapor interface (i.e., the surface tension of the ink) is set by the print head requirements [15] and substrate treatments (e.g., UV-ozone [34], plasma [35], chemical coating [36]) have to be used to modify the degree of wetting. The different wetting conditions are shown in the lower part of Figure 7. The spreading of the droplet should be minimized to achieve high-resolution printing. However, printing uniform structures on non-wetting substrates ($\theta \gg 90°$) is challenging and the optimal wetting conditions can be found at below $90°$ contact angle.

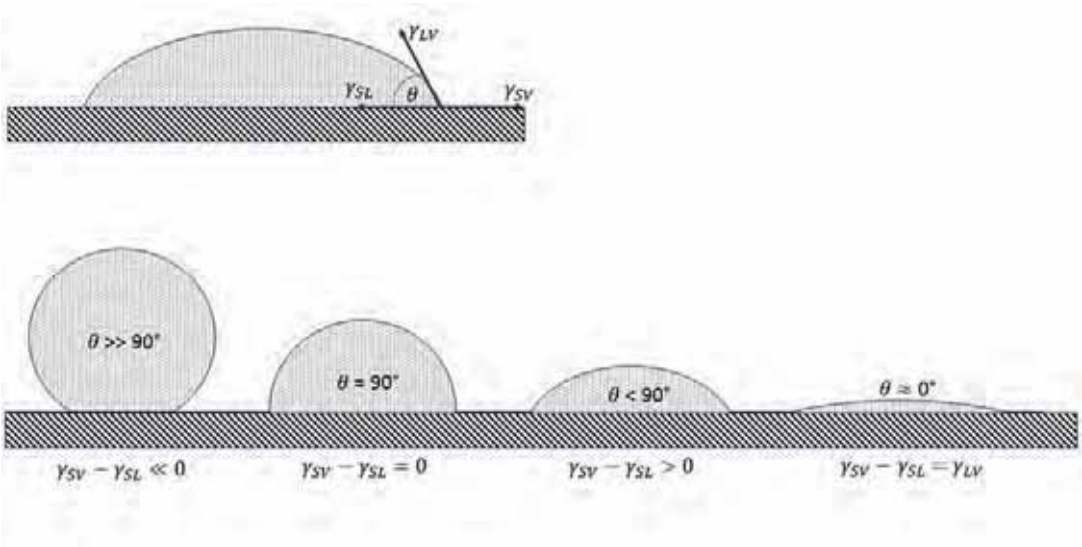

Figure 7: Equilibrium wetting of a droplet on a surface (upper part) and the different wetting conditions from non-wetting on the left, to complete wetting on the right (lower part). The θ is the contact angle, γ_{SV} is the surface energy of the solid-vapor interface, γ_{SL} is the surface energy of the solid-liquid interface and γ_{LV} is the surface energy of the liquid-vapor interface.

However, real substrates and inks are non-ideal and therefore enable contact line at a non-equilibrium contact angle [37]. This may be a result of a non-homogenous chemical composition or a local variation of the roughness in the substrate. It is also possible that the fast evaporation of the solvent after the impact of the droplet and subsequent deposition of solid particles on the contact line causes this type of behavior [37]. In part due to these reasons, it is highly challenging to take direct contact angle measurements for functional inks on real substrates, and for these reasons, the effect of surface treatment is often measured by observing the size of the deposited droplets with the fiducial camera of the printer.

2.5.2 Line width, edge and surface roughness

The line width, edge roughness and surface roughness are mainly determined by the spreading of deposited droplets in relation to the distance between center points of subsequent droplets (i.e., drop spacing) and the time delay between their deposition (see Figure 8). If the drop spacing is larger than the diameter of the deposited droplet isolated droplets will form (a); when the drop spacing is reduced, droplets start to merge, and scalloping starts to occur (b); with a further reduction in drop spacing a uniform line forms (c); followed by bulging line (d). If the time delay between the deposition of subsequent droplets is longer than the drying time of a droplet, a stacked coins structure forms (e). In general, the edge roughness of a line is at maximum in the case of scalloping or bulging lines and lines with a stacked coin structure. Furthermore, the substrate temperature affects the starting point of different line morphologies. [38]

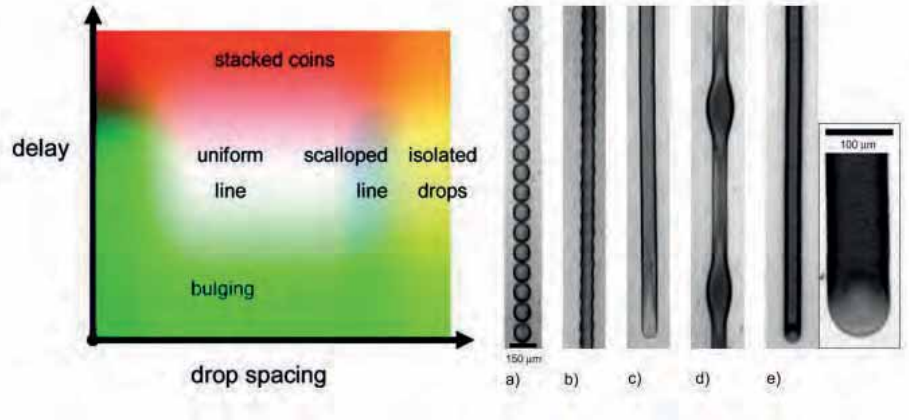

Figure 8: Dependence of DoD inkjet printed line morphologies on drop-spacing and time delay (left part) and examples of different line morphologies (right part). See text for explanations [38], © American Chemical Society.

The discussion above applies to both piezoelectric inkjet and E-jet printers. However, in E-jet printers the line morphology is also affected by the small volume and charging of the droplets. The charging of the droplet may reduce the resolution because the charge separation inside the droplet can cause the droplet to break in-flight and lead to the formation of small satellite droplets which increase the edge roughness of the printed line (see Figure 9, left part) [42].As the volume of the droplet is reduced from picolitre to femtolitre size, the evaporation rate becomes more significant due to the high surface area to volume ratio. Firstly, this reduces the time delay where a stacked coin structure can be avoided. Secondly, since functional inks consist of a solid material (e.g., nanoparticles) dispersed in a solvent, the increased solvent evaporation relative to the droplet volume causes the effective solid content to increase thereby leading to increased viscosity of the droplet [39]. This reduces the spreading velocity and the resulting droplet diameter [40].

As shown in reference [41], another specific challenge in E-jet printing is that the thickness of the solid material deposited by the droplet is very small because it is proportional to the diameter of the droplet. For example, in the case of 5 µm wide lines printed with Ag-nanoparticle ink NPS-J (Harima Chemicals, Japan), the first layer is only 50 nm thick (see Figure 9, right part) which is too thin to provide a sufficient number of conductive paths through the nanoparticle matrix to form a conductor. Multilayer printing, therefore, has to be used to increase the conductor's cross-sectional area. For 2 and 5 µm wide conductors 5 to 10 layers are required to form a conductive line and 25 to 30 layers are required to minimize the conductor resistance. However, the multilayer printing leads to the accumulation of nanoparticles on the centreline of the conductor thereby increasing the surface roughness of the conductor (see Figure 9, right part).

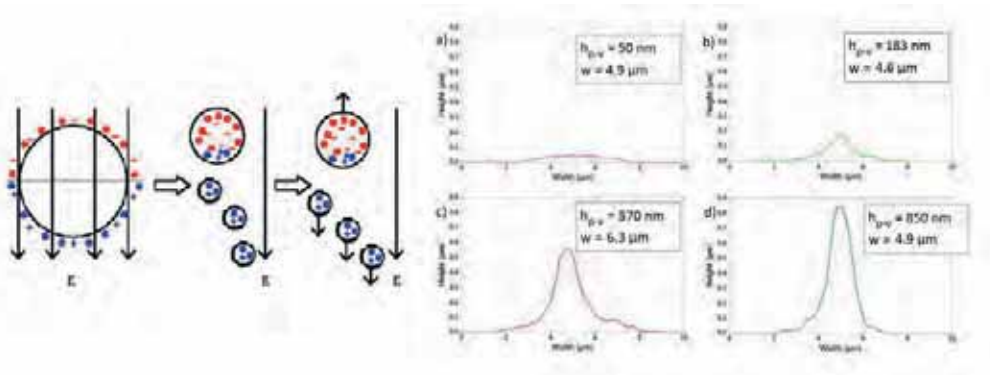

Figure 9: Droplet charging and break-up in-flight (left part, © 2010 American Institute of Physics) and morphologies of E-jet printed multilayer lines (right part from [41], © 2015 IEEE).

The high-precision printing capability depends mainly on the alignment accuracy of the printer and the edge-roughness of the printed conductor. The effect of the substrate non-idealities (e.g. local surface energy differences) on the edge-roughness can be suppressed by choosing chemically homogenous substrate; for example, in **Publication V**, where piezoelectric inkjet printed S/D-electrodes with ~10 µm channel length were required, the substrate was fabricated by chemical vapour deposition of Parylene C to reach suitable level of substrate homogeneity. In this case, the limiting factor is not the substrate, but the alignment accuracy of the piezoelectric inkjet printer (± 5 µm). For E-jet printing, however, the limiting factor will be the edge-roughness of the conductor resulting from the aforementioned formation of satellite droplets due to charging of the ejected droplets. As shown in the **Publication I,** this effect can be reduced to certain extent by adjusting the print height. However, the electrical characteristics of the substrate seem to also affect the generation of the satellite droplets thereby making the E-jet high-precision patterning capability highly application specific.

2.6 Functional inks for digital fabrication

The materials employed in electronics can be categorized according to their electrical functionality into conductive, semi-conductive and dielectric types. In printed electronics, these functionalities can be achieved with various ink types: for example, conductive features can be printed with metal nanoparticle [43], metal-organic decomposition (MOD) [44], graphene [45] or doped polymer inks [47], while semi-conducting features may be fabricated, for example, with organic small-molecule polymer blends [48], or inorganic metal oxide inks [49]. Because of the large number of material options for each functionality, this chapter concentrates mainly on the functioning principles and processing conditions of materials employed in the publications of this thesis. In addition to the aforementioned three “main” functionalities, the sub-category of piezoelectric dielectric materials is introduced because it is related to the fabrication of a monolithically printed sensor-amplifier system.

2.6.1 Conductive inks

Silver and gold nanoparticle inks are the most common commercially available conductive metal-based inks. The main benefits of these inks are their relatively low sintering temperature (< 150C for Ag-ink [50]), which allows the use of cheap, low glass transition temperature polymer substrates such as polyethylene terephalate (PET); higher solid content (30 to 60 wt% [50]) compared to MOD inks (10 to 20 wt% [51]) which allows the formation of thicker, higher conductance traces; and significantly higher conductivity compared to doped polymer inks. Silver and gold nanoparticle based inks were employed in all publications of this thesis. [52][53]

Metal nanoparticle inks are comprised of nanoparticles a few tens of nanometres in diameter dispersed in solvent and capped with organic stabilizers. The purpose of the stabilizer is to prevent the agglomeration of the particles prior to the sintering step, while the solvent rheology (e.g., the viscosity and surface tension) is optimized for the specific printing technology to ensure the printability of the ink. During the sintering step, the ink is heated so that the solvent evaporates, and the nanoparticles are brought into contact with each other (see Figure 10, left part). This is followed by the decomposition of the organic stabilizer, which must be completely removed to induce coarsening (i.e., Ostwald ripening [54]) of the nanoparticle structure and the concomitant formation of conductive paths through the nanoparticle matrix. Ostwald ripening is driven by surface and grain boundary diffusion, which first leads to the formation of a neck between the particles (see Figure 10, right part). In general, the diffusion direction is from particles with a smaller radius towards particles with a larger radius [54]. The diffusion stops once the particle radius reaches a critical value (approximately 1.5 times the original particle size) and at this point the conductivity reaches its maximum value. The resulting structure remains porous and this leads to lower conductivity when compared to bulk metal: for example, commercial silver nanoparticle resistivities range from 2 to 12 μΩ*cm [50], while the resistivity of bulk silver is 1.47 μΩ*cm [55]. However, these values are significantly lower than can be achieved with a doped polymer such as poly(3,4-ethylenedioxythiophene):poly(styrenesulfonate) (PEDOT:PSS), which has a resistivity in the mΩ*cm range [56]. The process time for the sintering step depends on the ink type and method of heat transfer. While a convection oven is the most commonly used method, it suffers from a long process time and relatively high process temperature [43] [57]. For this reason, alternative faster heat transfer methods such as laser, plasma, rapid electrical sintering, and photonic sintering have been investigated [43] [58]. [52] [53]

Figure 10: Left part: nanoparticles dispersed in solvent with a stabilizer layer (0), heating for solvent evaporation and decomposition of the stabilizer layer (1) and coarsening of the nanoparticle structure (2) [24]. Right part: diffusion mechanisms affecting the coarsening of the nanoparticle structure [52], © Royal Society of Chemistry.

2.6.2 Dielectric inks

Insulating structures between conductors can be formed by employing dielectric inks. The dielectric ink utilized in this thesis was an organic UV-curable epoxy resin (**Publication II**). In general, the UV-curable organic dielectric inks consist of monomers and/or oligomers dispersed in a solvent, which also contains photoinitiators. After deposition of the material, the structure must be heated to evaporate the solvent. This is followed by exposure to UV-light of sufficient intensity and energy dose. The UV-light activates the photoinitiators, which react with the monomers and/or oligomers thereby inducing a polymerization reaction, which leads to the formation of a cross-linked polymer structure. The chemical and temperature stability of the insulating layer can be increased with a final, higher temperature heating step. [53]

2.6.3 Piezoelectric inks

Ferroelectric dielectrics are materials which have a permanent electric polarization (i.e., a net surface charge in the absence of an external electric field) arising from the internal electric dipoles of the crystal structure. A mechanical deformation of the crystal structure will cause a change in the strength of the dipoles, and therefore, a change in the net surface charge. Similarly, the internal dipoles will be affected by a change in the surface charge (i.e., by a change in the external electric field) which will result in a mechanical deformation of the crystal structure. The first phenomenon is called the *direct* piezoelectric effect and it is often utilized in energy harvesting applications [61] and sensor applications for sensing pressure [62] or bending [63]. The second phenomenon is called the *indirect* piezoelectric effect and it is utilized in various actuators such as the piezoelectric element of the inkjet print head discussed earlier [15]. However, the most common piezoelectric materials are polycrystalline, and do not exhibit piezoelectric behavior in their pristine form because the ferroelectric crystal domains are randomly oriented so that the net electric dipole moment across the sample is zero. An external electric field (i.e., a poling field) is then required to re-orient the ferroelectric domains to induce spontaneous polarization. [59] [60]

Most piezoelectric inks are based on copolymers of poly(vinylidenefluoride) (P(VDF)) such as poly(vinylidenefluoride-trifluoroethylene) (P(VDF-TrFE)) utilized in **Publications V and VI**. The P(VDF-TrFE) consists of crystallites embedded in amorphous regions and similarly to inorganic polycrystalline ferroelectrics, it requires a poling field to induce the piezoelectric effect [59]. In general, the required poling field is significantly higher when compared to inorganic ferroelectrics, such as lead zirkonium titanate PZT (100 V/µm vs. 1-2 V/µm) [59] [90]. Despite this, the intrinsic piezoelectric sensitivity is lower (e.g., d_{33} = 30 pC/N vs. d_{33} = 400-500 pC/N) [64][90]. However, the processing temperature of P(VDF-TrFE) is also significantly lower than that of the PZT (~135 °C vs ~550 °C) [65][90] and it is soluble in common solvents (e.g., 2-butanone, dimethylformamide), which makes it better suited for printed electronics applications. Compared to PVDF, the P(VDF-TrFE) has the benefit of not requiring any stretching during the poling step, which makes it possible to apply it directly on top of the electrode in solution form. [59]

3 Applications of high-precision inkjet printing

This chapter introduces the different applications in the field of electronics packaging, transistor interconnects and amplifier printing, where the digital high precision printing technologies add new functionalities to existing processes or result in completely new functionalities which cannot be achieved with conventional electronics fabrication processes.

3.1 Electronics packaging

Silicon interposers enable the 3D-integration of multiple functionalities in a single electronics package (e.g., System-in-Package, SiP) by acting as a mechanical and signal interface between the multiple stacked devices and the printed circuit board (PCB). This approach results in miniaturized package dimensions and shorter connections between the devices, thereby leading to lower power consumption and signal latency, and a higher operating speed [66]. State of the art silicon interposers are able to bridge the pitch gap between the high density I/Os of the device and the low density I/Os of the package by employing a high-density redistribution layer (RDL) consisting of W/S < 10/10 µm conductors in two or more metallization layers separated by dielectric and connected with microvias with a diameter of less than 20 µm (see Figure 10, left part) [4][67]. These structures are currently fabricated using lithographic methods, which contain multiple process steps (e.g., metal plating; applying and exposing the photoresist; developing; removing the photoresist) thus resulting in inflexible processes with a high degree of material consumption. The selective metallization and dielectric deposition using contactless digital printing technologies therefore has the potential to increase the flexibility of the RDL fabrication process and reduce its environmental impact. The required < 10/10 µm should be well within the capabilities of E-jet printing while the higher throughput piezoelectric inkjet printer could be used for the deposition of the large-area dielectric layer.

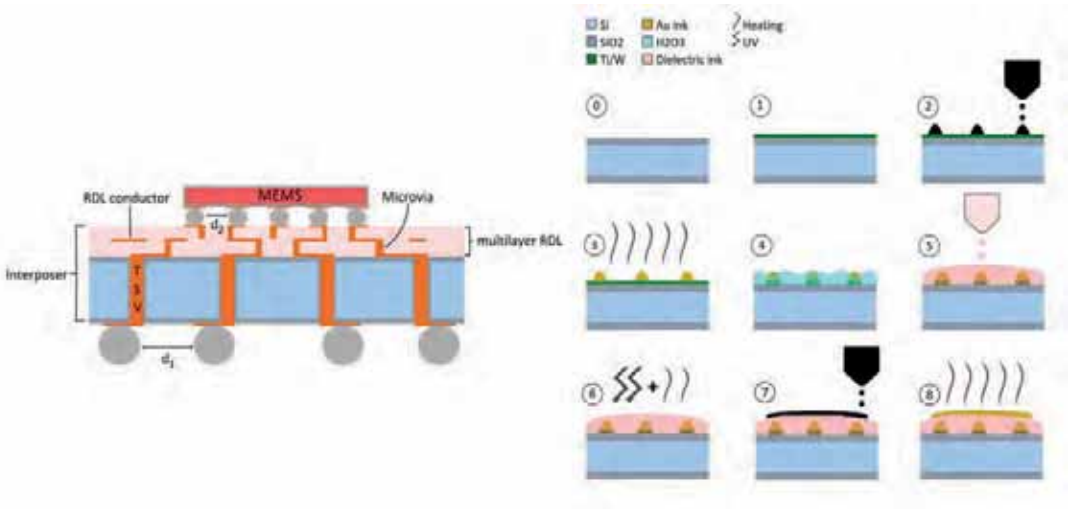

Figure 11: High-density multilayer RDL (left part) and printing process (right part) (from **Publication III**), © 2017 IEEE.

In **Publication II, the** combination of E-jet and piezoelectric inkjet printing was studied for the fabrication of a high-density RDL of a silicon interposer with a 5/5 µm W/S circuitry in two metallization layers separated by a dielectric and connected with a microvia approximately 10 µm in diameter. Gold nanoparticle ink AU-Nanometal (ULVAC, Japan) was used for E-jet printing the conductors and microvia pillar, while a UV-curable epoxy based dielectric RUV-4001 (SIJ Technology, Japan) was used for the piezoelectric inkjet printing of the dielectric layer. The E-jet printing stability was first investigated by depositing interdigitated and meander electrodes with 5/5 µm W/S in both metallization layers (MET1 and MET2) and measuring for short and open circuits. The printing process for these structures is shown in Figure 11. Prior to printing, the silicon wafer was sputtered with Ti/W to provide an adhesion layer between the substrate and the printed Au-conductors (1). This was followed by E-jet printing (2) and sintering (3) the MET1 conductors. The etching of the Ti/W layer (4) was the only non-additive part in the process and it should be possible to replace this by adding an adhesion promoter for SiO2 in the Au-ink formulation. The dielectric layer was printed by a piezoelectric inkjet printer (5) and cured (6) followed by E-jet printing (7) and curing (8) the MET2 conductors. For comparison, the lithographic fabrication process of a 2.5D interposer may contain as many as 20 separate process steps [46].

During the E-jet printing process, it was possible to use a high droplet ejection frequency for the MET1 conductors, which resulted in higher resolution patterning (as shown in **Publication I**). However, for printing the MET2 conductors the print parameters (i.e. amplitude and bias voltages, the print frequency and print speed) had to be re-calibrated because the dielectric substrate affected the strength of the electric field and therefore the droplet volume. Furthermore, the MET2 conductors had to be printed with a bipolar voltage so that the subsequent droplets would have the opposite

charge to prevent charging the dielectric substrate. This limited the maximum droplet ejection frequency and reduced the resolution so that the conductor width was over 5 µm in the MET2 and only ~2 µm in the MET1 conductors (Figure 12, right part). Despite these challenges, it was possible to demonstrate stable jetting in both metallization layers (Figure 12, left part). Multilayer printing for the conductors was employed to achieve a high aspect ratio and reduce the resistance of otherwise high resistivity nanoparticle conductors. This approach enabled printing of MET1 and MET2 conductors with a maximum aspect ratio of ~3.5 and ~1, respectively. The resistivity of the MET1 conductors corresponded well with the datasheet value of 8 µOhm*cm, but for the MET2 conductors it was significantly higher at ~45 µOhm*cm. It was hypothesized that the higher resistivity of the MET2 layer could be related to insufficient thermal treatment of the dielectric layer or the large coefficient of a thermal expansion (CTE) mismatch between the gold (14 ppm/K [68]) and epoxy (45 to 65 ppm/K [69]) which may result in delamination and cracking of the gold conductors. In conclusion, the results indicated that the signal routing of a high density printed RDL should be done preferably in MET1 conductors instead of MET2 conductors.

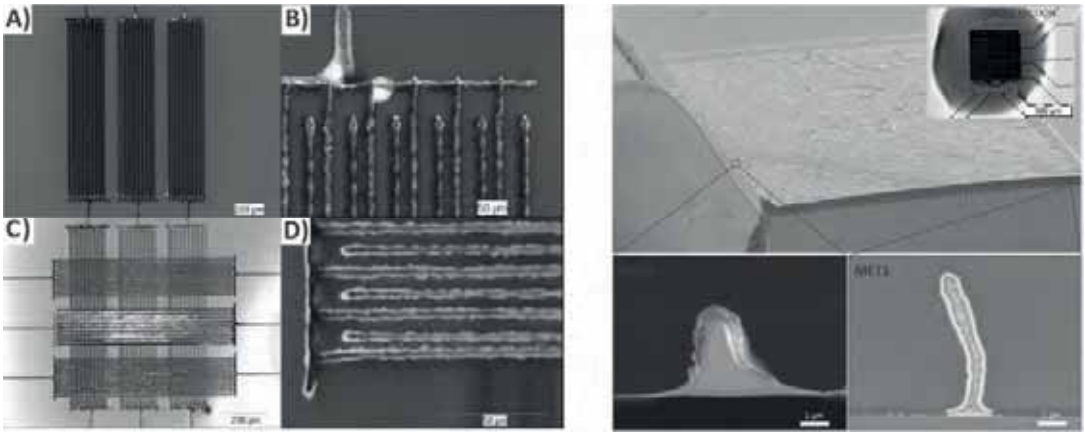

Figure 12: Left part: high-density RDL MET1 conductors (A and B) and MET2 conductors (C and D). Right part: SEM images of MET1 and MET1 cross-sections (from **Publication II**), © 2017 IEEE.

The E-jet printing of micropillars was utilized in the fabrication of the microvia interconnect between the MET1 and MET2 conductors. E-jet micropillar printing is based the fast evaporation of small diameter droplets due to the large droplet surface area to volume ratio. For sub-femtoliter volume droplets the evaporation rate is fast enough that a significant volume of solvent evaporates in-flight and multiple droplets can be printed one top of each other resulting in the formation of a micropillar. In the study, the printing voltage (bias voltage + amplitude) was optimized so that the resulting pillar had a diameter of approximately 10 µm, which is two times smaller than the current industry standard. The pillar height was controlled by adjusting the total jetting time. The pillar aspect ratio ranged from 4 to 11 with a minimum resistance of 360 mOhm. Images of the printed micropillars are shown in Figure 13.

The resistance range of the RDL depends on the application field. For example radio frequency (RF) devices require resistance values of under 10 mOhm, but lower frequency applications allow resistances up to 1kOhm and electromagnetic interference (EMI) shielding can be done even at 1 MOhm [70]. Considering the demonstrated resistance values for fully printed high-density RDL conductors, the maximum path lengths would be ~1100 µm in MET1 and ~110 µm in MET2 if the RDL is to be utilized for radio frequency (RF) applications. These values should be sufficient to redistribute some signal paths from package I/Os to device I/Os, but likely not all. Therefore, it is expected that the application area for fully printed RDLs would be in the field of lower frequency devices, which can be found, for example, in MEMS packaging. Compared to other fully printed high density redistribution layers fabricated for example with aerosol printing [28], the results presented in this contribution show a 2 to 4 fold increase in wiring density and ~10 fold decrease in via diameter.

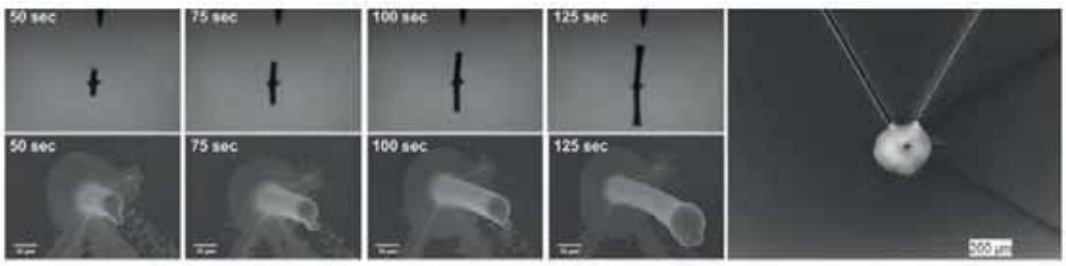

Figure 13: E-jet printed micropillar and microvia (from **Publication II**), © IEEE 2017.

Outside the work done for this thesis, the digital and additive fabrication in electronics packaging has been demonstrated in the metallization of large diameter TSVs [71] [72], as well as in the dielectric filling of TSVs [73] and the fabrication of under bump metallization (UBM) [73]. Furthermore, the metallization of high-density TSVs, which are a vital part of the silicon interposer and which utilise high density RDLs, has been investigated using high-resolution E-jet printing [74]. In these studies, it was found that the metallization and dielectric filling of TSVs is feasible with digital additive fabrication technologies. However, the TSV metallization with piezoelectric inkjets require multiple heating steps for solvent evaporation due to the low volumetric solid content of the nanoparticle inks. In the case of E-jet metallized high-density vias, the number of evaporation steps could be reduced due to the evaporation of small volume droplets already in-flight.

3.2 Transistor interconnects

Application specific printed circuits (ASPECs) are related to application specific integrated circuits (ASICs) in that they both contain circuits customized for a specific instead of general use (e.g., ICs

or RAM). However, ASPECs employ digital printing technologies instead of semiconductor fabrication processes to achieve at-home/office personalization (i.e., field-configurability) of the pre-fabricated gate arrays. Specifically, the lithographically fabricated gate arrays form unconnected logic blocks with interconnect resources in the top-most metallization layer, while the printing technologies are used to configure these interconnections in the field and depending on the application. Compared to roll-to-roll or screen printing, the inkjet printing technologies offer a natural solution in terms of field-configurability due to the highly customizable process flow resulting from the use of digital print files instead of physical print masks. Inkjet printing technologies also provide easier accessibility due to their more compact size and simple print file and print head preparation. Similar to ICs or ASICs fabricated with conventional semiconductor processes, the ASPEC performance (e.g., processing speed and energy consumption) scales with the array density and circuit complexity. Because high-resolution lithographic methods are used for the array implementation, the resolution of inkjet printing technologies is the limiting factor in achieving high interconnect and array density and concomitant high performance of ASPEC circuits. [75]

In **Publication III** E-jet and aerosol jet (AJ) printing were compared for metallizing high-density ASPEC interconnects. The test vehicles consisted of photolithographically pre-fabricated Au-conductors in the bottom and top metallization layer (MET1 and MET5, respectively) separated by two passivation layers with 10 µm² and 16 µm² area vias on top of the MET1 conductors (see Figure 14). The MET5 conductors were connected to the I/O pads and the MET1 conductors formed via-to-via interconnects, while the different printing technologies were utilized in the fabrication of the MET1-to-MET5 interconnection in MET6. In real ASPEC circuits, the MET1 conductors would be used to connect the transistor electrodes in the gate array and the MET6 printed interconnects would be used to configure the connections between the gate arrays to fit the user-determined application. The photolithography process for the OTFT fabrication enables gate lengths of approximately 4 µm, which determines the transistor size and array density. The printed conductor line width has to conform to this density requirement to fully maximize the performance of the ASPEC circuit. It is therefore important to achieve minimum line width printed interconnects; however, this should not come at the cost of the interconnect yield. In the study, E-jet printed conductors with designed conductor widths of 6, 12 and 20 µm were printed in MET6 and their sheet resistance and yield were compared with aerosol jet printed 15 µm and photolithographically fabricated 9 µm wide conductors.

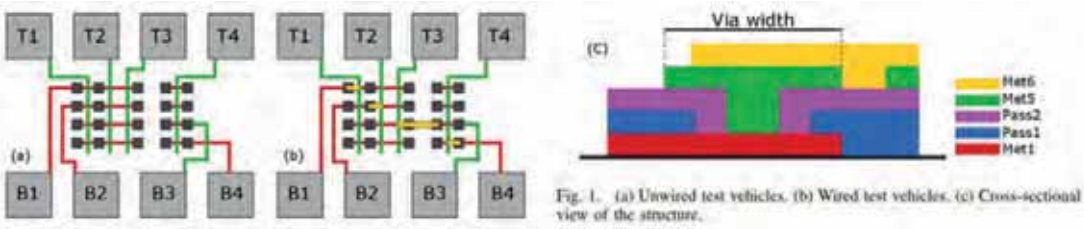

Fig. 1. (a) Unwired test vehicles. (b) Wired test vehicles. (c) Cross-sectional view of the structure.

Figure 14: ASPEC gate array and interconnect test vehicle structures (from **Publication III**), © 2016 IEEE.

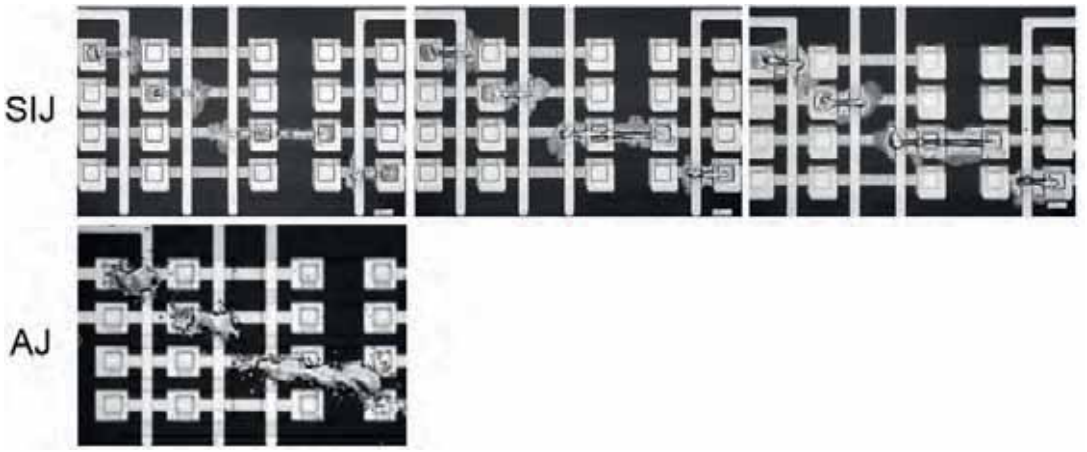

Figure 15: ASPEC structures with SIJ printed 6, 12 and 20 µm (upper part) and AJ printed 15µm interconnects (lower part) (from **Publication III**), © 2016 IEEE.

The results indicated that the E-jet printed 20 µm wide interconnects have a yield of 88%, while the AJ printed and photolithographically fabricated conductors had a yield of 72% and 97%, respectively. Comparing the E-jet and AJ printed conductors (Figure 15 upper part vs. lower part, respectively), it was apparent that the yield was both a function of the conductor uniformity and positioning accuracy of the printing device. The E-jet was also able to form interconnects at smaller line width compared to AJ technology, thus indicating that it is the better option to fully maximize the performance of ASPEC circuits.

In **Publication IV** E-jet printing and piezoelectric inkjet (IJ) printing were compared for ASPEC interconnect fabrication. A photolithographically pre-fabricated circuit was optimized so that a single IJ droplet could be used to form the interconnect between the bottom metallization layer (MET1) and intermediate metallization layer (MET2) in the top metallization layer (MET3) (see Figure 16, left part). For E-jet printing the optimized structure allowed the use of a bumping method, whereby each bank was filled with multiple ink layers with a certain time delay between the layers leading to the relatively fast build-up of thick, low resistance interconnects in MET3. In the study, the resistance of the printed interconnects was compared to the photolithographically fabricated counterpart and the interconnect yield was related to the via density by metallizing 50, 60, 70 µm width (W) vias with 30, 40, 50 µm via-to-via spacing (S) (see Figure 16, right part and Figure 17, left part).

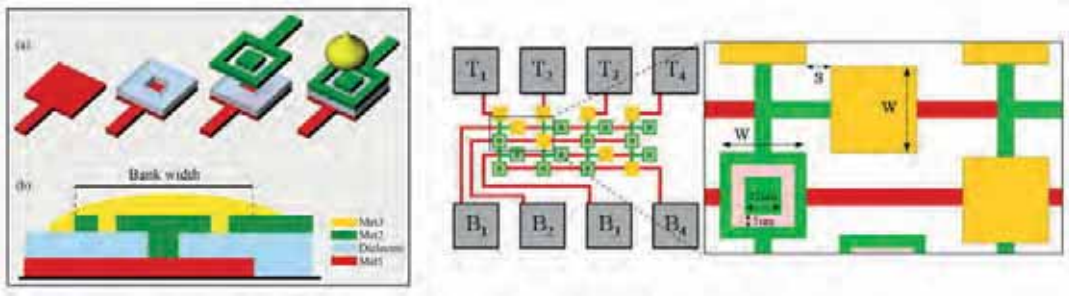

Figure 16: The ASPEC interconnect resource optimized for inkjet droplets (left part) and interconnect resource dimensions (right part) (from **Publication IV**), © 2017 IOP Science.

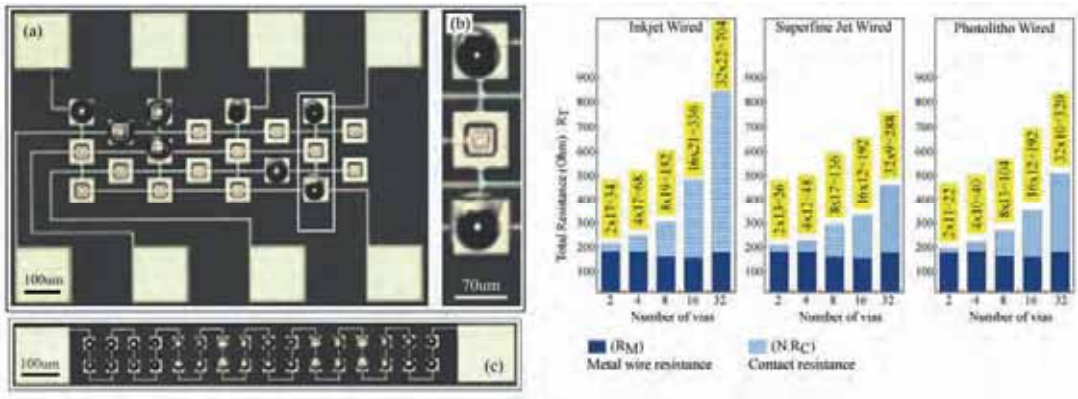

Figure 17: E-jet metallized ASPEC interconnects (left part) and a comparison of the resistance for E-jet, AJ and photolithography metallized via-chains (right part) (from **Publication IV**), © 2017 IOP Science.

The total resistance R_T of the wired via-chains is shown in the left part of Figure 17 decomposed to its resistive components i.e. the metal wire resistance R_M (dark blue section of the bars) and total contact resistance of the vias NR_T (pale blue section of the bars), where the N indicates the number of vias in the via-chain. For convenience, the total contact resistance of the vias is calculated above the bars. The contact resistance of single via R_C can be then calculated by dividing the total contact resistance of the via-chain by the number of vias. The via-resistance of the E-jet printed interconnects (12.6 Ohm) was comparable to the photolithographically fabricated counterpart (11.2 Ohm) and significantly lower than that of the IJ printed interconnects (19.2 Ohm) (see Figure 17, right part). The yield of the E-jet printed interconnects could be increased significantly through the use of an optimized interconnect resource structure and a 100% yield could be achieved for 40 and 50 µm via-to-via spacing, while the 30 µm via-to-via spacing included a few short circuits between the vias. However, it should be possible to increase the yield by more careful optimization of the print parameters. Although the IJ printing was able to produce a comparable yield to E-jet printing, the larger droplet size of the IJ printer will ultimately limit the via diameter to ~30 µm, while the E-jet printing

can be utilized for significantly smaller vias due to the smaller droplet size (see **Publication I**). However, at the time of the experiments, the lack of low sintering temperature inks with stable E-jet jetting limited its applicability to connect OTFT based ASPEC circuits. Thus, only the effect of IJ printed interconnects on the operating frequency of an OTFT based ring oscillator circuit could be investigated. Ten IJ interconnected ring oscillators had an average oscillation frequency of 54 kHz while the highest oscillation frequency was 74 kHz which compared well with photolithographically interconnected counterpart.

In conclusion, E-jet printing shows promise in interconnect fabrication of high-density, low resistance field-configurable ASPEC circuits. Especially promising is the printing on the bank structure optimized for piezoelectric inkjet droplets, since it reduces the process variation related to the conductor edge/surface roughness thereby increasing the yield. Furthermore, finding or formulating stable low-temperature E-jet inks is important to fully benefit from the high-resolution of the E-jet patterned interconnects for low temperature OTFT based ASPECs. The temperature resilient inorganic semiconductor based ASPECs should be compatible with high sintering temperature E-jet inks introduced in the previous publications. Although the piezoelectric inkjet printer shows promise due to its higher throughput, it may lead to compromises in the array density and performance of the ASPEC due to its lower resolution.

3.3 Miniaturization of a lab-on-skin system through monolithic integration

In the previous chapters, high-precision digital printing technologies were used to enhance and bring new functionalities to existing fabrication processes without making sacrifices in the level of miniaturization. However, they can be also used for fabrication of systems which enable completely new functionalities that do not have existing counterparts in conventional electronics fabrication. The monitoring of human health conditions with ultra-thin printed biosignal measurement systems is an example of such an application. In the future, these lab-on-skin systems could contain all the necessary components for biosignal acquisition, amplification, powering and data transfer and enable patients to be monitored unobtrusively.

Figure 18: Proposed ultra-thin lab-on-skin setup with printed piezoelectric biosignal sensor and integrated charge amplifier.

3.3.1 Ultra-thin biosignal amplifier with integrated passive components

Monolithically integrated circuits contain both large and small area structures (e.g., capacitors and transistors) and are therefore not optimal for low throughput E-jet printing. For example, E-jet printing a 200 nm thick 1 mm² square electrode for a parallel plate capacitor takes approximately 7 minutes assuming 5-micron diameter droplets, a 1 kHz droplet ejection frequency, a 50% overlap between droplets and a single layer thickness of 50 nm, whereas the same task can be accomplished with a piezoelectric inkjet printer in the order of few tens of seconds. For transistor printing, however, small feature sizes are required. The switching speed of the field effect transistor is described by the equation for transition frequency:

$$f_t = \frac{\mu_s}{2\pi L^2}(V_{GS} - V_{TH})^2$$

where μ_s is semiconductor mobility, L is the channel length, V_{TH} is the threshold voltage and V_{GS} is the gate-to-source voltage. Thus, the switching speed of the transistor can be increased by adjusting the semiconductor mobility μ_s, or by adjusting the transistor channel length L. Because the organic semiconductor mobilities are limited to relatively low values (rubrene μ_s = ~20 cm/Vs [76]), it is necessary to increase the switching speed by minimizing the channel length. The high droplet positioning accuracy (+/- 5 µm, see Table 2) of the piezoelectric printer should be sufficient for fabrication of a ~10 µm source/drain electrode gap (i.e. channel length) transistor. Furthermore, because the throughput of the piezoelectric inkjet printer is relatively high compared to E-jet printing, a small channel length transistor *and* large area integrated parallel plate capacitor could be fabricated in the same process. Together with the development of direct printed organic semiconductor inks, this would allow the fabrication of monolithically integrated printed circuits, which would have sufficient performance for certain low frequency applications found in the field of on-skin biosignal monitoring.

For example, the arterial pulse wave (PW) used for diagnosis of various vascular diseases contains relevant information in a narrow frequency band of 50 mHz - 50Hz [91].

Regarding the on-skin biosignal monitoring, the ultra-thin form factor of the amplifier is important for achieving high skin conformability and enhanced user comfort without the use of adhesives. Inkjet printing technologies offer a natural solution to this problem because the nanoparticle inks employed in conductor fabrication generally have a low volumetric solid content [50] and therefore low deposited material thickness (~1% of the droplet diameter, see Figure 9). Due to the lack of inkjet printable organic semiconductor inks, dispensing technology is often used for the deposition of the active material of the transistor because it allows for a wider range of rheological properties while still maintaining the highly customizable process flow due to the use of digital print files [77] [78]. Furthermore, the solid content of the dispensing inks can be reduced so that the requirement for an ultra-thin form factor is not jeopardized. The main shortcoming of the dispensing technology, its low resolution, is not highly significant for printing transistors because the transistor performance is not affected by the horizontal dimensions of the semiconducting layer.

In **Publication V,** piezoelectric inkjet printing and dispensing were utilized for the fabrication of ultra-thin (~3 µm thick) organic pseudo-CMOS inverter-based charge amplifiers with monolithically integrated passive components (i.e., bias/feedback resistors and parallel plate feedback capacitor). The S/D electrodes, gate, resistor/capacitor electrodes and component interconnects were metallized with an inkjet printer while the high-resistivity resistor material and active material of the transistor were dispensed. Chemical vapor deposition of parylene was utilized for the substrate, parallel plate capacitor dielectric and gate dielectric fabrication to achieve thin and highly controllable layer thicknesses. The amplifier was characterized by measuring the voltage transfer characteristic (VTC) curves, small signal gain, amplitude and phase response. Furthermore, the capability of the amplifier for biosignal amplification was evaluated by using a pulse wave signal recorded from the radial artery on the wrist of a person (**Publication VI**) as an input signal and then comparing it to the output.

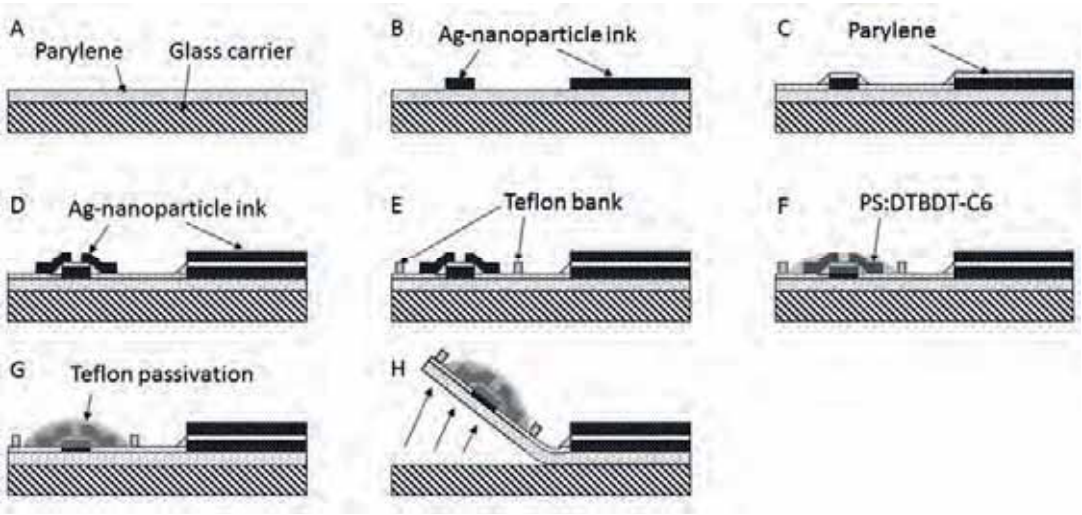

Figure 19: Fabrication process of an ultra-thin charge amplifier. See text for process description.

The fabrication process for the charge amplifier is shown in Figure 19. For simplicity, the interconnects and resistor printing are omitted from this picture. First, the glass carrier substrate with release layer is coated with a one-micron parylene layer using chemical vapor deposition (A). This is followed by printing the gate and capacitor electrodes and interconnects in the first metallization layer using a piezoelectric inkjet printer and a low sintering temperature (~130 °C) Ag-nanoparticle ink, NPS-JL (Harima Chemicals, Japan) (B). A parylene layer of ~150 nm thickness is then deposited on the sample to form the gate and capacitor dielectric (C). This is followed by printing the transistor source/drain (S/D) and resistor electrodes and the capacitor top electrode with Ag-nanoparticle ink in the second metallization layer (D). The printing of S/D electrodes utilizes the highly controllable droplet positioning accuracy of the piezoelectric inkjet printer and homogenous substrate surface energy of the parylene to achieve an S/D gap (i.e., channel length) of ~10 µm. This is followed by dispensing a surface energy pattern with fluoropolymer (E), which is used to control the spreading of the dispensed high-resistivity resistor ink and the p-type organic semiconductor ink used as the transistor channel material (F). A fluoropolymer passivation layer is dispensed onto the transistors and resistors to prevent degradation of the respective materials (G). Finally, the amplifier can be carefully released from the carrier substrate (H). The final device is shown in Figure 20.

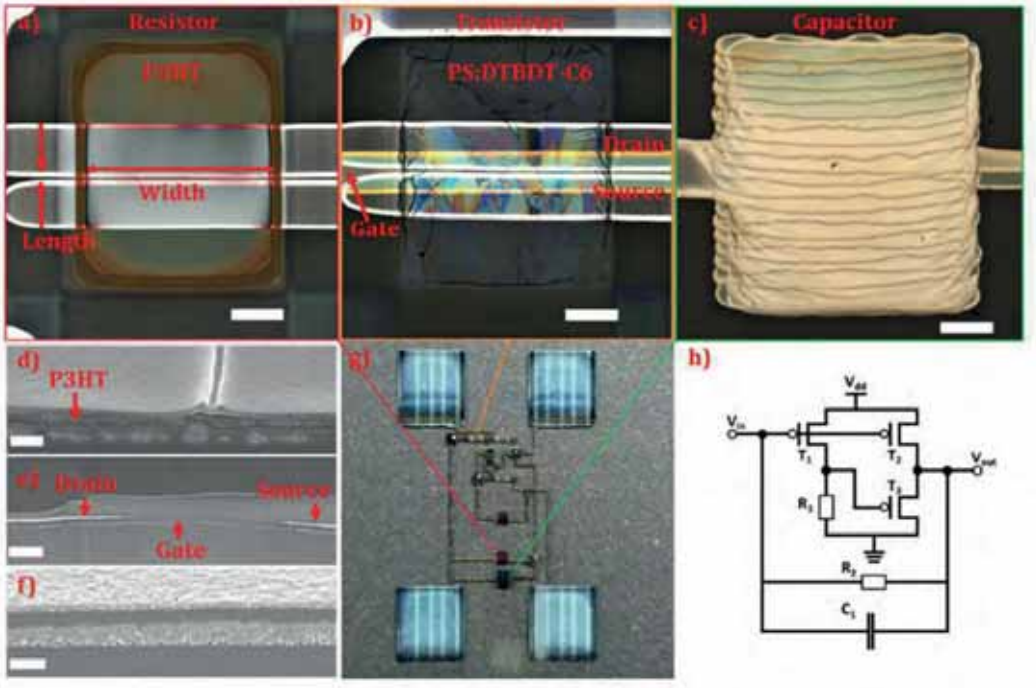

Figure 20: Ultra-thin charge amplifier (g, h) with an integrated bias/feedback resistor (a, d), feedback capacitor (c, f) and active components (b, e). The scale bars are 200 µm in a, b and c; and 200 nm, 2 µm and 400 nm in d, e and f, respectively (from **Publication V**), © 2019 IEEE.

The reproducibility of the amplifier fabrication was investigated by measuring the VTC of eight amplifiers and calculating the respective small signal gains (see Figure 21 a). The maximum small signal gain was ~14, while the coefficient of variation (CV) was 20%. The latter could be partially explained by the resistor fabrication process variation (CV = 9.4%). Furthermore, the feedback capacitor fabrication process had a low CV of 2.8%, which is especially important in order to achieve reproducible charge amplification because $A_{charge} \approx -1/C$. Compared to printed amplifier circuits fabricated with conventional passive components, the demonstrated fully printed amplifier achieved comparable operating voltage (5 V vs. 0.3 to 30 V) and voltage amplification (14 vs. 1.6 to 67.3) [78][79][80][81][82]. Furthermore, the amplifier passband could be adjusted to fit requirements of pulse-wave-based diagnostics by varying the value of the feedback resistance. The frequency responses, including charge and voltage amplification and respective phase responses, were measured for two amplifiers with high and low resistance value (see Figure 21 b). An amplifier with 60 MHz to 32 Hz optimized passband was chosen to amplify a PW-signal recorded with a poly(vinyldenefluoride-co-trifluoroethylene) (P(VDF-TrFE)) based piezoelectric pressure sensor from the radial artery on a person's wrist (see Figure 21 c). The clinically relevant indices were calculated from the sensor signal and amplifier output and then compared. After removing the high frequency

noise component from the amplifier output, the differences in the parameter values were no greater than the variation caused by changing physiological factors.

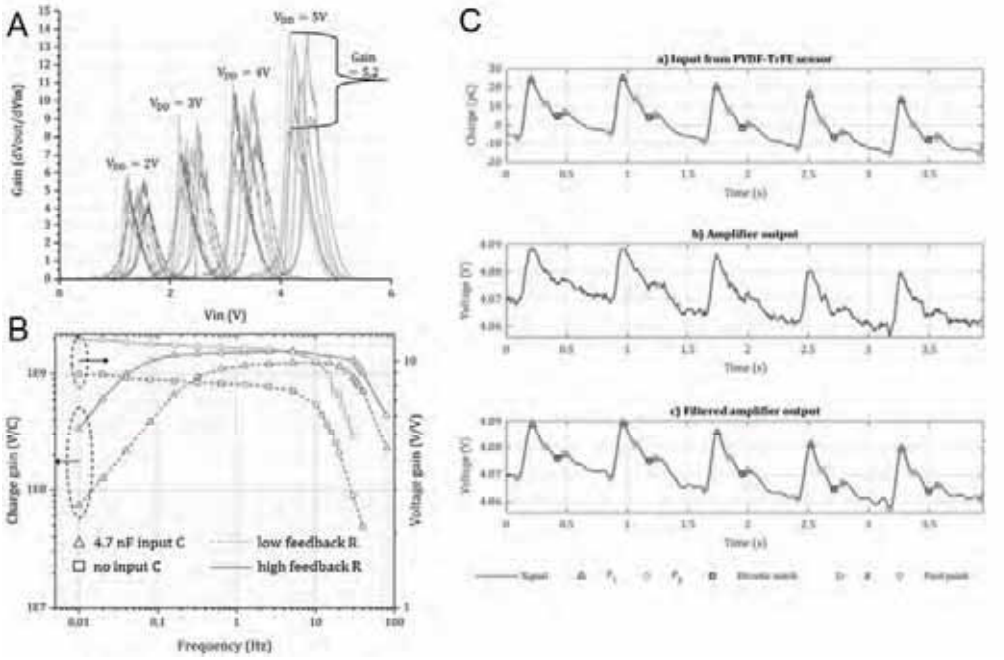

Figure 21: Small signal gain (A), frequency response (B) and pulse wave amplification (C) of the amplifier (from **Publication V**), © 2019 IEEE.

In conclusion, the demonstrated monolithic integration of active and passive components with a combination of high precision and low precision digital printing technologies indicates that they are promising candidates for the miniaturization of printed electronic circuits. Furthermore, monolithic integration could be achieved with a relatively small reduction in the process throughput because the large area parallel plate capacitor electrodes and small area S/D electrode gap were fabricated in the same inkjet printing process. This is especially important in the case of ultra-thin devices, which would probably be disposable due to their fragility, and which need to be therefore affordable. The alternative option for fabricating such structures with E-jet based process would reduce the S/D-gate electrode overlap and would be likely to lead to improved transistor performance, but also significantly reduce the throughput (as discussed in the beginning of this chapter) thereby increasing the fabrication cost. Furthermore, certain applications of on-skin biosignal measurements can be successfully performed at relatively low frequencies (as shown above) so that high-performance transistors are not necessarily required. If however a higher transistor performance would be needed, a hybrid fabrication based on piezoelectric inkjet and E-jet printing could be applied, whereby the

S/D-gate electrode overlap is reduced by printing only the bottom gate with an E-jet printer and other circuit features with a piezoelectric inkjet.

3.3.2 Printed piezoelectric P(VDF-TrFE) pulse wave sensor

In future, the demonstrated ultra-thin amplifiers could be used to amplify the biosignal from a monolithically fabricated sensor. Together with integrated antennas for data-transfer and an energy supply for powering the active elements [83] [84], these components could form an independent lab-on-skin setup and lead to the miniaturization of the whole measurement system [85]. Sensors based on organic piezoelectric materials (e.g., PVDF, P(VDF-TrFE)) offer a convenient approach to the measurement of biosignals which can be detected via mechanical deformation (e.g., pressure or strain). Due to their low processing temperature and solution processability, they would also enable the use of low temperature, ultra-thin, biocompatible substrates (e.g., parylene or PET) and the use of printing tools to meet the affordability requirement discussed earlier. Furthermore, the self-generation of a transduced signal via the piezoelectric effect (i.e., the generation of a charge in response to mechanical deformation) would lead to lower energy consumption compared to sensors utilizing other transduction mechanisms, such as capacitive or piezoresistive effects [59].

The blood pulse pressure wave travelling through the radial arteries is a prime example of a biosignal which could be detected using the aforementioned physical sensors. Parameters calculated based on the shape of the pulse wave (PW) can be related to the arterial elasticity, which has been used as an indicator for several cardiovascular diseases (CVDs) such as hypertension, stroke, heart failure and myocardial infarction [86] [87]. The affordable and reliable at-home screening of these diseases enabled by printed piezoelectric sensors could have a significant social impact as CVDs are among the most common causes of death in the world. The detection of the pulse wave can be done by pushing the sensor element against the artery (i.e., by measuring the normal force) or, potentially, from the bending of the skin above the artery (i.e., by measuring the normal force and strain) [63]. The first option is well suited for thick, semi-rigid films, which can be easily attached to an external sensor housing, while the second option requires an ultra-thin form factor to allow for the bending of the piezoelectric element along with the skin. Previous studies have shown that it is indeed possible to fabricate P(VDF-TrFE) based pressure sensors which can measure the PW to a certain extent [88], but the accuracy and reliability of the PW signal has not been validated with statistical methods. This is an important step to be accomplished before the development of an ultra-thin monolithically integrated amplifier sensor system.

In **Publication VI** the signal quality of a printed P(VDF-TrFE) based PW sensor was evaluated in a pre-clinical study using statistical methods. The sensor was fabricated on a 125 µm thick PET substrate; however, in the future the goal is to transfer the fabrication process to a thinner 1.4 µm PET substrate [89]. The fabrication process is pictured in Figure 22. First, the bottom electrode is printed

using a piezoelectric inkjet printer with Ag-nanoparticle ink and sintered (A). This is followed by bar coating of the P(VDF-TrFE) layer and subsequent curing (B). Screen printing is used for the fabrication of the top electrode from a PEDOT:PSS conductive polymer (C). The P(VDF-TrFE) layer is polarized to induce more surface charges and increase the sensitivity of the sensor (D). Finally the sensor is coated with a parylene passivation layer to prevent degradation of the PEDOT:PSS conductive polymer (E). The monolithic integration of the sensor to the amplifier element should be possible with these printing technologies assuming that the sensor is printed and polarized prior to printing the amplifier. It should be also noted that inkjet printable PEDOT:PSS and P(VDF-TrFE) inks exist and these could be used instead of screen printing and bar coating to keep to the overall theme of achieving a highly customizable digital process flow.

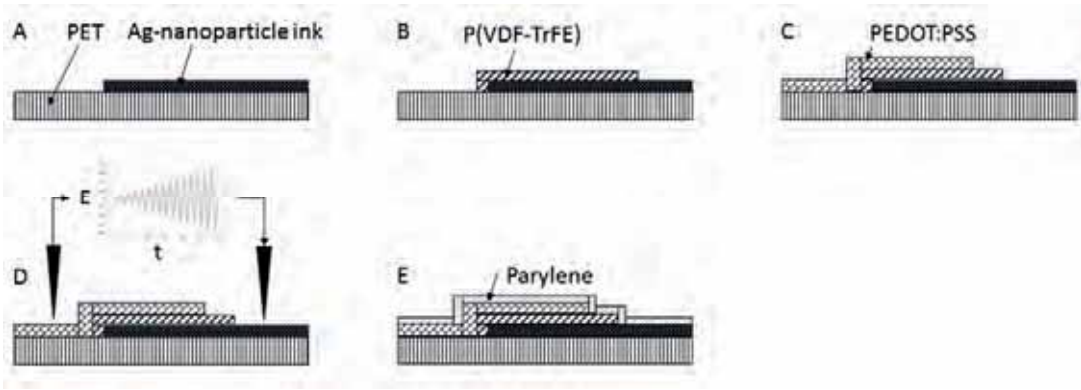

Figure 22: Fabrication process for a P(VDF-TrFE) based PW sensor. See text for process description.

The bar coated P(VDF-TrFE) layer has a relatively low mean thickness of only 9.5 ± 0.8 µm for 8 samples, while the total thickness of the inkjet/screen printed electrodes is in the order of 0.5 µm (see Figure 23 c) resulting in a total MIM-stack thickness of ~11 µm. Based on the 0.8 µm standard deviation for the P(VDF-TrFE) layer thickness, it should be possible to reduce the layer thickness to ~3 µm without a significant reduction in the yield assuming a polarization voltage of 80 V/µm and dielectric strength of 400 V/µm [90]. Together with a 1.4 µm PET foil, a 3 to 4 µm MIM stack thickness should be enough to meet the < 5 µm thickness requirement for an ultra-thin setup. The P(VDF-TrFE) layer was further characterized by measuring the remanent polarization (7.3 µC/cm², 3 samples) and the effective piezoelectric coefficient $d_{33,f}$ (-26.9 ± 2.9 pC/N, 10 samples), which compared well to the literature values of 7.0 µC/cm² and -25 pC/N, respectively (see Figure 21 f). It must be noted that the $d_{33,f}$ measurement may contain additional contribution from other piezoelectric coefficients activated by multidirectional forces, and that the material d_{33} may therefore differ from the measured effective value. However, the effect of multidirectional forces during the PW measurement (discussed more thoroughly in the next paragraph) cannot be ruled out and a transverse piezoelectric coefficient may also affect the sensor sensitivity there.

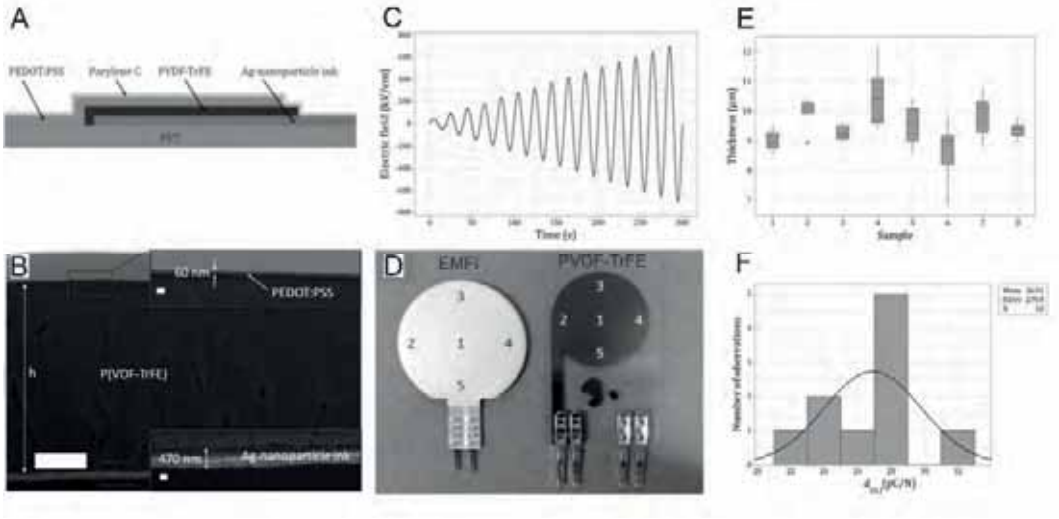

Figure 23: A P(VDF-TrFE) PW-sensor structure (A and B), poling waveform (C), EMFi and P(VDF-TrFE) sensors with $d_{33,f}$ measurement excitation points (D), P(VDF-TrFE) PW sensor thickness of 8 samples (E) and effective piezoelectric coefficient $d_{33,f}$ of 10 samples (F) (from **Publication VI**).

During the PW measurement the P(VDF-TrFE) sensor was installed in a sensor housing together with a previously validated, electromechanical film (EMFi) based PW sensor [91] and the setup was attached against the radial artery on a number of patients' wrists (see Figure 24, left). The PW of 20 patients were measured and clinically relevant indices were calculated based on the obtained signal from both sensors (see Figure 24, middle and right). The agreement between the two sensors was then evaluated using common statistical methods. According to the results, the two PW sensors were in strong agreement for the stiffness index (SI), while moderate agreement was found for the radial augmentation index (rAIx). However, the agreement for the reflection index (RI) was slightly over the limit. It was hypothesized that the placement of measurement setup might vary between the patients and this could cause multidirectional forces to be exerted on the P(VDF-TrFE) – EMFi sensor stack. Since the P(VDF-TrFE) is sensitive to multidirectional forces and the EMFi sensor is only sensitive to the normal force, poor sensor placement would only affect the parameters calculated based on the P(VDF-TrFE) generated signal.

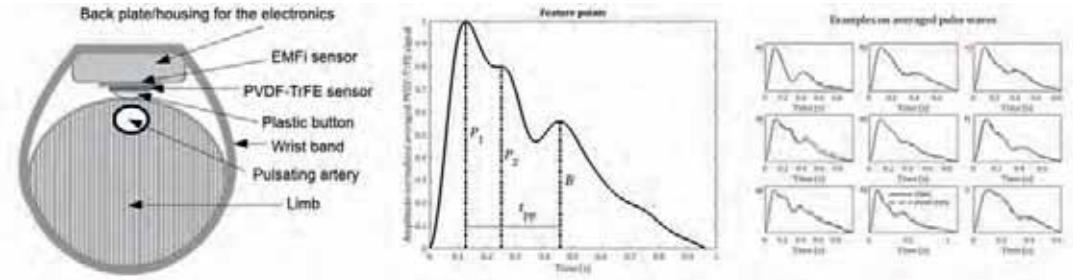

Figure 24: PW measurement setup (right), PW feature points used for calculation of relevant indices (middle) and PW measurement signal comparison of EMFi and printed PVDF-TrFE sensors (right) (from **Publication VI**), © IEEE 2019.

Prior to this study, printed PW-sensors had been demonstrated [92][93][94], but the validity and reliability of the PW signal generated by them had not been studied with statistically significant sample sizes, or with the use of a reference PW-sensor. In this contribution, the additive fabrication of a P(VDF-TrFE) based piezoelectric PW sensor was demonstrated and the signal quality was validated in a pre-clinical study against a state-of-art PW sensor. The results showed that the sensor could be used for measuring certain clinically relevant PW indices such as the pulse peak time difference, RI and rAIx. The hypothesized shear force induced noise in the P(VDF-TrFE) sensor provides motivation to develop an ultra-thin pulse wave sensor with a more direct coupling between the measured phenomenon (bending of skin) and the sensor.

4 Concluding remarks

Continuous improvements in lithographic fabrication processes towards higher resolution and monolithic integration have led to the development of highly miniaturized silicon based electronic devices. This has resulted in increased operating speeds, lower energy consumption and smaller package sizes, which together have enabled the ubiquitous adoption of electronics into our every-day lives. The printed electronics fabrication processes suffer from limited resolution and it is therefore unlikely that they will achieve a similar scale of miniaturization. However, as demonstrated in this thesis, there are multiple application fields where pushing the envelope of digital printing technologies towards higher resolution and higher levels of miniaturization results in increased and, in some cases, completely new functionalities.

In electronics packaging **(Publications I and II)**, the feasibility of E-jet and piezoelectric inkjet printing was demonstrated in fabrication of a high-density RDL with comparable resolution to current lithographic methods. The resulting highly customizable process flow could enable faster and more cost-effective prototyping and small batch package fabrication compared to lithographic fabrication methods with high tooling costs. This would also enable wafer level fabrication of customized RDLs. It would also reduce the environmental impact through reduced material consumption and the use of less hazardous processing chemicals. As demonstrated, these benefits would come without sacrifices in the I/O-density and the size of the package. Compared to other fully printed high density redistribution layers fabricated for example with aerosol printing, these results show a 2 to 4 fold increase in wiring density and ~10 fold decrease in via diameter.

In application specific integrated printed circuit (ASPEC) fabrication **(Publications III and IV)**, E-jet printing was shown to result in comparable resolution to other high-precision printing technologies, thereby demonstrating the field-configurability of the gate arrays without sacrifices in their density or concomitant processing speed. Comparison between printing technologies and lithographic method is not necessarily sensible, because field-configurability is enabled by digital printing technologies and would not be possible to achieve with lithographic methods due to tooling requirements. However, it may be speculated that there is the potential to increase the array density so it would be closer to lithographically fabricated ASICs by employing interconnect resources optimized to take the full advantage of the femtoliter E-jet droplets.

The monolithic integration of printed active and passive components on ultra-thin, biocompatible substrates with digital printing technologies enables the fabrication of highly skin-conformable devices for biosignal amplification: in **Publication V,** an all printed ultra-thin charge amplifier was demonstrated. Again, this type of functionality through the miniaturization of the device thickness is enabled by printing technologies alone and cannot be achieved with conventional active/passive components due to their physical size and rigidity. A direct performance comparison between the

conventional and demonstrated amplifier is therefore not valid. However, it was shown that the performance of the all printed amplifier is sufficient for amplification of an arterial pulse wave signal with sufficient detail to determine clinically significant parameters. The high-precision printing technologies used therefore enable completely new functionalities in human health monitoring which have not existed before. Compared to printed amplifier circuits fabricated with conventional passive components, the demonstrated fully printed amplifier achieves comparable operating voltage (5 V vs. 0.3 to 30 V) and voltage amplification (14 vs. 1.6 to 67.3).

In the future, the thickness of the PW sensor generating the biosignal should be also miniaturized so that the whole system (i.e. amplifier + sensor) could be monolithically fabricated on the same ultra-thin substrate. However, before attempting this, the accuracy and reliability of the biosignal generated by the pressure sensor should be validated **(Publication VI)**. The last publication in this thesis shows, that it is indeed possible to generate a reliable PW signal with a piezoelectric pressure sensor fabricated with printing tools. These results pave the way for miniaturization of the entire biosignal monitoring system. Prior to this study, printed PW-sensors have been demonstrated, but the validity and reliability of the PW signal generated by them has not been studied with statistically significant sample sizes, or with the use of a reference PW-sensor.

References

[1] Moore G., “Progress in Digital Integrated Electronics,” in Technical Digest International Electron Devices Meeting. IEEE, 1975, pp. 11-13

[2] Dennard R. H., Gaensslen, F. H., Rideout V. L., Bassous E., LeBlanc A. R., “Design of ion-implanted MOSFET’s with very small physical dimensions”, IEEE Journal of Solid-State Circuits, 9(1974)5, pp. 256-268

[3] Kilby J. S. “Invention of Integrated Circuit”, IEEE Transactions on Electron Devices, 23(1976)7, pp. 648-654

[4] Tummala R. R. ”System on Package: Miniaturization of the Entire System, Chapter 9: MEMS Packaging”, McGraw-Hill Professional, 2008

[5] Intel Corp. “Intel 14nm Technology”, [Online], Accessed: https://www.intel.com /content/www/us/en/silicon-innovations/intel-14nm-technology.html [Accessed: 11.03.2019]

[6] Robertson J. “High Dielectric Constant Oxides”, The European Physical Journal – Applied Physics, 28(2004)3, pp. 265-291

[7] Suganuma K. “Introduction to Printed Electronics”, Springer, 2014

[8] Fukuda K., Someya, T. “Printing Technology: Recent Progress in the Development of Printed Thin-Film Transistors and Circuits with High-Resolution Printing Technology”, Advanced Materials, 29(2017)25, pp. 1602736

[9] van Osch T. H. J., Perelaer J., de Laat A. W. M., Schubert U. S., “Inkjet Printing of Narrow Conductive Tracks on Untreated Polymeric Substrates” Advanced Materials, 20(2007)2, pp. 343-345

[10] McKerricher G., Perez J. G., Shamim A. “Fully Inkjet Printed RF Inductors and Capacitors Using Polymer Dielectric and Silver Conductive Ink with Through Vias”, IEEE Transactions on Electron Devices, 62(2015)3, pp. 1002-1009

[11] Jung S., Sou A., Gili E., Sirringhaus H., “Inkjet-Printed Resistors with a Wide Resistance Range for Printed Read-Only Memory Applications”, Organic Electronics, 14(2013)3, pp. 699-702

[12] Kwon J., Takeda Y., Fukuda K., Cho K., Tokito S., Jung S., “Three-Dimensional, Inkjet-Printed Organic Transistors and Integrated Circuits with 100% Yield, High Uniformity, and Long-Term Stability”, ACS Nano, 20(2016)11, pp. 10324-10330

[13] Chang S.-C., Liu J., Bharathan J., Yang Y., Onohara J., Kido J., “Multicolor Organic Light-Emitting Diodes Processed by Hybrid Inkjet Printing”, Advanced Materials, 11(1999)9, pp. 734-737

[14] Thuau D., Kallitsis K., Dos Santos F. D., Hadziioannou G., “All inkjet-printed piezoelectric electronic devices: energy generators, sensors and actuators”, RSC Journal of Material Chemistry, (2017)5, pp. 9963-9966

[15] Hutchings I. M., Martin G. D., “Inkjet Technology for Digital Fabrication”, Wiley, 2013

[16] Pekkanen V, Mäntysalo M., Kaija K., Mansikkamäki P., Kunnari E., Laine K., Koskinen S., Halonen E., Caglar U., ”Utilizing inkjet printing to fabricate electrical interconnections in a system-in-package”, Microelectronic Engineering, 11(2010)87, pp. 2382-2390

[17] Davis A. W., Agarwal K., “Radio Frequency Circuit Design: Appendix F, Transistor and Amplifier Formulas”, Wiley, 2001

[18] “Fujifilm Dimatix Printhead Reference Chart”, Fujifilm, [Online]. Available: https://www.fujifilmusa.com/products/industrial_inkjet_printheads/printproducts/printheads/index.html#general-purpose

[19] Kim S.-Y., Kim K., Hwang Y. H., Park J., Jang J., Nam Y., Kang Y., Kim M., Park H. J., Lee Z., Choi J., Kim Y., Jeong S., Bae B.-S., Park J.-U. “High-resolution electrohydrodynamic inkjet printing of stretchable metal oxide semiconductor transistors with high performance”, Nanoscale 8(2016), pp. 17113-17121

[20] Han Y., Wei C., Dong J., “Super-resolution electrohydrodynamic (EHD) 3D printing of micro-structures using phase change inks”, Manufacturing Letters, 2(2014)4, pp. 96-99

[21] Li X., Park H., Lee M. H., Hwang B., Kim S. H., Lim S., “High resolution patterning of Ag nanowire flexible transparent electrode via electrohydrodynamic jet printing of acrylic polymer-silicate nanoparticle composite overcoating layer”, Organic Electronics, 62(2018), pp. 400-406

[22] Onses M. S., Sutanto E., Ferreira P. M., Alleyne A. G., Rogers J. A., “Mechanisms, Capabilities and Applications of High-Resolution Electrohydrodynamic Jet Printing”, Small, 11(2015)34, pp. 4237-4266

[23] Lee A., Jin H., Dang H. W., Choi K. H., Ahn K. H., “Optimization of Experimental Parameters to Determine the Jetting Regimes in Electrohydrodynamic Printing”, Langmuir, 29(2013)44, pp. 13630-9

[24] Laurila M. M., “Super Inkjet Printed Redistribution Layer For a MEMS Device”, Tampere University of Technology, 2015

[25] Park J., Kim B., Kim S. Y., Hwang J., “Prediction of Drop-on-Demand (DoD) Pattern Size in Pulse Voltage Applied Electrohydrodynamic (EHD) Jet Printing of Ag-nanocolloid Ink”, Applied Physics A, 117(2014)4, pp. 2225-2234

[26] Renn M. J., “Direct Write System”, US Patent 718894B2, 2006

[27] Mette A., Richter P. L., Hörtels M., Glunz S. W., “Metal Aerosol Jet Printing for Solar Cell Metallization”, Progress in Photovoltaics, 15(2007)7, pp. 621-627

[28] Cai F., Chang Y.-H., Wang K., Zhang C., Wang B., Papapolymerou J., “Low-Loss 3-D Multilayer Transmission Lines and Interconnects Fabrication by Additive Manufacturing Technologies”, 64(2016)10, pp. 3208-3216

[29] Mahajan A., Frisbie C. D., Francis L. F., “Optimization of Aerosol Jet Printing for High-Resolution, High-Aspect Ratio Silver Lines”, ACS Applied Materials and Interfaces, (2015)5, pp. 4856-4864

[30] Wilkinson N. J., Smith M. A. A., Kay R. W., Harris R. A., “A Review of Aerosol Jet Printing – A Non-Traditional Hybrid Process for Micro-Manufacturing”, The International Journal of Advanced Manufacturing Technology, (2019), pp. 1-21

[31] Optomec, “Aerosol Jet Technology”, [Online], Available: https://www.optomec.com/printed-electronics/aerosol-jet-technology/ [Accessed: 24.06.2019]

[32] Paulsen J. A., Renn M., Christensson K, Plourde R., “Printing Conformal Electronics on 3D Structures with Aerosol Jet Technology”, in 2012 FIIW Proceedings, Gattinburg, TN, USA

[33] de Gennes P.-G., Brochard-Wyart F., Quere D., “Capillarity and Wetting Phenomena”, Springer, 2004

[34] Efimenko K., Wallace W. E., Genzer J., “Surface Modification of Sylgard-184 Poly(dimethyl siloxane) Networks by Ultraviolet and Ultraviolet/Ozone Treatment”, Journal of Colloid and Interface Science 254(2002)2, pp. 306-315

[35] Bhattacharya S., Datta A., Berg J. M., Gangopadhyay S., “Studies on Surface Wettability of Poly(dimethyl)siloxane (PDMS) and Glass Under Oxygen-Plasma treatment and Correlation with Bond Strength”, Journal of Microelectromechanical Systems, 14(2005)3, pp. 590-597

[36] Lee S.-H., Shin K.-Y., Hwang J. Y., Kang K. T., Kang H. S., “Silver Inkjet Printing with Control of Surface Energy and Substrate Temperature”, Journal of Micromechanics and Microengineering, 18(2008)7, p. 075014

[37] Deegan R. D., Bakajin O., Dupon T. F., Huber G., Nagel S. R., Witten T. A., “Contact Line Deposits in an Evaporating Drop”, Physical Review E, 62(2000)1, pp. 756-765

[38] Soltman D., Subramanian V., “Inkjet-Printed Line Morphologies and Temperature Control of the Coffee Ring Effect”, Langmuir, 24(2008)5, pp. 2224-2231

[39] Konjin B. J., Sanderink O. B. J., Kruyt N. P., “Experimental Study of the Viscosity of Suspensions: Effect of Solid Fraction, Particle Size and Suspending Liquid”, Powder Technology, 266(2014), pp. 61-69

[40] Eddi A., Winkels K. G., Snoeijer J. H., “Short Time Dynamics of Viscous Drop Spreading”, Physics of Fluids, 25(2013), p. 013102

[41] Laurila M.-M., Soltani A., Mäntysalo M., ”Inkjet Printed Single Layer High-Density Circuitry for a MEMS Device” in 2015 ECTC, San Diego, CA, USA, pp. 968-972

[42] Yudistira H. T., Nguyen V. D., Dutta P., Byun D., ”Flight Behavior of Charged Droplets in Electrohydrodynamic Inkjet Printing”, Applied Physics Letters, 96(2010), p. 023503

[43] Niittynen J., Abbel R., Mäntysalo M., Perelaer J., Schubert U. S., Lupo D., “Alternative sintering methods compared to conventional thermal sintering for inkjet printed silver nanoparticle ink”, Thin Solid Films, 556(2014), pp. 452-459

[44] Shin D.-H., Woo S., Yem H., Cha M., Cho S., Kang M., Jeong S., Kim Y., Kang K., Piao Y, “A self-reducible and alcohol-soluble copper-based metal–organic decomposition ink for printed electronics”, ACS Applied Materials and Interfaces, 6(2014)5, pp. 3312-3319

[45] Li J., Ye F., Vaziri S., Muhammed M., Lemme M. C., Östling M., ”Efficient inkjet printing of graphene”, 25(2013)29, pp. 3985-3992

[46] Sun Y., Jin Z., Luo J., Li J., Sun Y., Wang Y., Ding G., “Modeling and Fabrication of the Redistribution Layer on the 2.5D Si-interposer”, in 2017 18th ICEPT, Harbin, China, pp. 157-161

[47] Eom S., Senthilarasu S., Uthirakumar P., Yoon S. C., Lim J., Lee C., Lim H. S., Lee J., Lee S.-H., “Polymer solar cells based on inkjet printed PEDOT:PSS layer”, Organic Electronics, 10(2009), pp. 536-542

[48] Shiwaku R., Matsui H., Nagamine K., Uematsu M., Mano T., Maruyama Y., Nomura A., Tsuchiya K., Takeda Y., Fukuda T., Kumaki D., Tokito S., “A printed organic amplification system for wearable potentiometric electrochemical sensors”, Scientific Reports, 8(2018), p. 3922

[49] Meyers S. T., Anderson J. T., Hung C. M., Thompson J., Wager J. F., Keszler D. A., “Aqueous inorganic inks for low-temperature fabrication of ZnO TFTs”, Journal of the American Chemical Society, 130(2008)51, pp. 17603-7609

[50] Advanced Nanoproducts, “Materials for microcircuit / printed electronics: Silver Jet Ink”, [Online], Available: http://anapro.com/eng/product/silver_inkjet_ink.html [Accessed: 26.04.2019]

[51] Perelaer J., Hendriks C. E., de Laat A. W. M., Schubert U. S., “One-step inkjet printing of conductive silver tracks on polymer substrates”, Nanotechnology 20(2009), p. 165303

[52] Perelaer J., Smith P. J., Mager D., Soltman D., Volkman S. K., Subramanian V., Korvink J. G., Schubert U. S. “Printed electronics: the challenges involved in printing devices, interconnects and contacts based on inorganic materials”, Journal of Materials Chemistry, 20(2010), pp. 8446-8453

[53] Magdassi S., “The chemistry of inkjet inks”, World Scientific Publishing Company, 2009

[54] Baldan A., “Review: progress in Ostwald ripening theories and their applications to nickel-base superalloys”, Journal of Materials Science, 37(2002), pp. 2171-2202

[55] Matula R. A., “Electrical resistivity of copper, cold, palladium and silver”, Journal of Physical and Chemical Reference Data, 8(1979)4, pp. 1147-1298

[56] Kim Y. H., Sachse C., Machala M. L., May C., Müller-Meskamp L., Leo L., “Highly conductive PEDOT:PSS electrode with optimized solvent and thermal post‐treatment for ITO‐free organic solar cells”, Advance Functional Materials, 21(2011)6, pp. 1076-1081

[57] Halonen E., Viiru T., Ostman K., Cabezas A. L, Mäntysalo M., ”Oven sintering process optimization for inkjet-printed Ag-nanoparticle ink”, IEEE Transactions on Components, Packaging and Manufacturing Technology, 3(2013)2, pp. 350-356

[58] Allen M. L., Aronniemi M., Mattila T., Alastalo A., Ojanperä K., Suhonen M., Seppä H., ”Electrical sintering of nanoparticle structures”, 19(2008)17, p. 175201

[59] Heywang W., Lubitz K., Wersing W., “Piezoelectricity: Evolution and Future of a Technology”, Springer Verlag, 2008

[60] Nelson W. G., “Piezoelectric materials: Structure, Properties and Applications”, Nova Science Publishers, 2010

[61] Bhanavanasi V., Kumar V., Parida K., Wang J., Lee P. S., ”Enhanced piezoelectric energy harvesting performance of flexible PVDF-TrFE bilayer films with graphene oxide”, ACS Applied Materials and Interfaces, 8(2016)1, pp. 521-529

[62] Sharma T., Je S.-S., Gill B., Zhang J. X. J., “Patterning piezoelectric thin film PVDF–TrFE based pressure sensor for catheter application”, Sensors and Actuators A: Physical, 177(2012), pp. 87-92

[63] Rajala S., Schouten M., Krijnen G., Tuukkanen S., ”High Bending-Mode Sensitivity of Printed Piezoelectric Poly(vinylidenefluoride-co-trifluoroethylene) Sensors”, ACS Omega, 3(2018)7, pp. 8067-8073

[64] Guo Q., Cao G. Z., Shen I. Y., “Measurements of piezoelectric coefficient d33 of lead zirconate titanate thin films using a mini force hammer”, Journal of Vibration and Acoustics, 135(2013), p. 011003

[65] Song Y. J., Zhu Y., Desu S. B., “Low temperature fabrication and properties of sol-gel derived (111) oriented Pb(Zr(1-x)Ti(x))O3 thin films”, Applied Physics Letters, 72(1998)21, pp. 2686-2688

[66] Miettinen J., Mäntysalo M., Kaija K., Ristolainen E. O., ”System Design Issues for 3D System-in-Package (SiP)”, in 2004 ECTC, Las Vegas, NV, USA, pp. 610-615

[67] Ndip I. and Töpper M., “Professional development course 8: Fundamentals of electrical design and fabrication processes of interposers including their RDLs,” in ECTC 2015, San Diego, CA, USA, pp. 26–29

[68] Nix F. C., MacNair D., “The thermal expansion of pure metals: copper, gold, aluminum, nickel and iron”, Physical review”, 60(1941), pp. 597-605

[69] Super Inkjet Tech. “RUV-4001 Datasheet”, 2016

[70] Khorramdel B., “Additive and Digital Fabrication of 3D Interconnects in MEMS Packaging Using Printing Technologies”, Tampere University of Technology, 2018

[71] Khorramdel B., Mäntysalo M., “Inkjet Filling of TSVs with Silver Nanoparticle Ink”, in 2014 ESTC, Helsinki, Finland, DOI: 10.1109/ESTC.2014.6962741

[72] Khorramdel B., Mäntysalo M., “Fabrication and Electrical Characterization of Partially Metallized Vias Fabricated by Inkjet”, Journal of Micromechanics and Microengineering, 26(2016)4, p. 045017

[73] Khorramdel B., Liljeholm J., Laurila M.-M., Lammi T., Mårtensson G., Ebefors T., Niklaus F., Mäntysalo M., ”Inkjet Printing Technology for Increasing the I/O Density of 3D TSV Interposers”, Microsystems & Nanoengineering 3(2017), pp. 17002

[74] Khorramdel B., Laurila M.-M., Mäntysalo M., ” Metallization of High Density TSVs Using Super Inkjet Technology”, in 2015 ECTC, San Diego, CA, USA, pp. 41–45

[75] Mashayekhi M., “Inkjet-Configurable Gate Arrays. Towards Application Specific Printed Electronic Circuits”, Universitat Autonoma de Barcelona, 2016

[76] Fachetti A., “Semiconductors for organic transistors”, Materials Today, 10(2007)3, pp. 28-37

[77] Shiwaku R., Takeda Y., Fukuda T., Fukuda K., Matsui H., Kumaki D., Tokito S., “Printed 2V-operating organic inverter arrays employing a small-molecule/polymer blend”, Scientific Reports, 6(2016), p. 34726

[78] Shiwaku R., Matsui H., Hayasaka K., Takeda Y., Fukuda T., Kumaki D., Tokito S, ”Printed organic inverter circuits with ultralow operating voltages”, Advanced Electronic Materials, 3(2017)5, p. 1600557

[79] Ramon E., Martínez-Domingo C., Alcalde-Aragonés A., Carrabina J., “Development of a simple manufacturing process for all-inkjet printed organic thin film transistors and circuits,” IEEE Transactions on Emerging and Selected Topics in Circuits and Systems, 7(2017)1, pp. 161–170

[80] Fukuda K., Takeda Y., Yoshimura Y., Shiwaku R., Tran L. T., Sekine T., Mizukami M., Kumaki D., Tokito S. “Fully-printed high-performance organic thin-film transistors and circuitry on one-micron-thick polymer films,” Nature Communications, 4(2014), p. 4147

[81] Kang H., Kitsomboonloha R., Ulmer K., Stecker L., Grau G., Jang J., Subramanian V., “MHz-class printed HMO TFT and inverters on plastic using attoliter-scl HS gravure-print sub-μ gate electrodes,” Organic Electronics, 15(2014)12, pp. 3639–3647

[82] Feng L., Tang W., Zhao J., Cui Q., Jiang C., Guo X., “All-solution-processed low-voltage organic thin-film transistor inverter on plastic substrate,” IEEE Transactions on Electron Devices, 61(2014)4, pp. 1175–1180

[83] Caccami M. C., Hogan M. P., Alfredsson M., Marrocco G., Batchelor J. C., “A tightly integrated multilayer battery antenna for RFID epidermal applications,” IEEE Transactions on Antennas and Propagation, 66(2018), p. 16052

[84] Huang X., Liu Y., Kong G. W., Seo J. H., Ma Y., Jang K.-I., Fan J. A., Mao S., Chen Q., Li D., Liu H., Wang C., Patnaik D., Tian L., Salvatore G. A., Feng X.,

Ma Z., Huang Y., Rogers J. A., “Epidermal radio frequency electronics for wireless power transfer”, Microsystems and Nanoengineering, 2(2016), p. 16052

[85] Liu Y., Pharr M., Salvatore G. A., “Lab-on-skin: a review of flexible and stretchable electronics for wearable health monitoring”, ACS Nano, 11(2017), pp. 9614-9635

[86] O’Rourke M. F., Hashimoto J.. "Mechanical factors in arterial aging: a clinical perspective." Journal of the American College of Cardiology, 50(2007)1, pp.1-13

[87] O’Rourke M. F., Pauca A., Jiang X. H. “Pulse wave analysis.” British Journal of Clinical Pharmacology., 51(2001)6, pp. 507-522

[88] Sekine T., Sugano R., Tashiro T., Sato J., Takeda Y., Matsui M., Kumaki D., Dos Santos D. F., Miyabo A., Tokito S., “Fully-Printed Wearable Vital Sensor for Human Pulse Rate Monitoring Using Ferroelectric Polymer”, Scientific Reports, 8(2018), p. 4442

[89] PolyK Technologies, “Ultra-Thin Free-Standing PET Film 1.4 μm”, [Online], Accessed: http://www.polyk-lab.com/product-2101 [Accessed: 29.03.2019]

[90] Arkema Piezotech, “TDS Piezotecho FC Ink P”, [Online], https://www. piezotech.eu/en/Technical-center/Documentation/, [Accessed: 29.03.2019]

[91] Peltokangas M., Vehkaoja A., Verho J., Huotari M., Röning J., Lekkala J., “Monitoring Arterial Pulse Waves with Synchronous Body Sensor Network”, IEEE Journal of Biomedical and Health Informatics, 18(2014)6, pp. 1781-1787

[92] Luo N., Dai W., Li C., Zhou Z., Lu L., Poon C. C. Y., Chen S.-C., Zhang Y. and Zhao N., “Flexible piezoresistive sensor patch enabling ultralow power cuffless blood pressure measurement,” Advanced Functional Materials, 26(2015)8, pp. 1178-1187

[93] Park D.Y., Joe D. J., Kim D. H., Park H., Han J. H., Jeong C. K., Park H., Park J. G., Joung B., Lee K. J., “Self-powered real-time arterial pulse monitoring using ultrathin epidermal piezoelectric sensors”, Advanced Materials, 29(2017)37, p. 1702308

[94] Pang C., Koo J. H., Nguyen A., Caves J. M., Kim M.-G., Chortos A., Kim K., Wang P. J., Tok J. B.-H., Bao Z, “Highly skin-conformable microhairy sensor for pulse signal amplification”, Advanced Materials, 27(2015)4, pp. 634-640

PUBLICATION I

Statistical Analysis of E-jet print parameter effects on Ag-nanoparticle ink droplet size

Laurila M. M., Khorramdel B., Dastpak A., and Mäntysalo M

Journal of Micromechanics and Microengineering, 27(9), p. 095005
(https://doi.org/10.1088/1361-6439/aa7a71)

PUBLICATION II

Combination of E-Jet and Inkjet Printing for Additive Fabrication of Multilayer High-Density RDL of Silicon Interposer

Laurila M. M., Khorramdel B. and Mäntysalo M

IEEE Transactions on Electron Devices, 64(3), pp. 1217-1224
(10.1109/TED.2016.2644728)

PUBLICATION III

Evaluation of Aerosol, Superfine Inkjet, and Photolithography Printing Techniques for Metallization of Application Specific Printed Electronic Circuits

Mashayekhi M., Winchester L., Louise E., Pease T., Laurila M.-M., Mäntysalo M., Ogier S., Teres L. and Carrabina J.

IEEE Transactions on Electron Devices, 63(3), pp. 1246-1253
(10.1109/TED.2016.2522388)

PUBLICATION IV

Chip-by-Chip Configurable Interconnection Using Digital Printing Techniques

Mashayekhi M., Winchester L., Laurila M.-M., Mäntysalo M., Ogier S., Teres L. and Carrabina J.

Journal of Micromechanics and Microengineering, 27(4), p. 0450009
(https://doi.org/10.1088/1361-6439/aa5ef3)

PUBLICATION V

A Fully Printed Ultra-Thin Charge Amplifier for On-Skin Biosignal Measurements

Laurila M.-M., Matsui M., Shiwaku R., Peltokangas M., Verho J., Montero L. K., Sekine T., Vehkaoja A., Oksala N., Tokito S. and Mäntysalo M.

IEEE Journal of Electron Device Society, 7, pp. 566-574
(DOI 10.1109/JEDS.2019.2915028)

PUBLICATION VI

Evaluation of Printed P(VDF-TrFE) Pressure Sensor Signal Quality in Arterial Pulse Wave Measurement

Laurila M.-M., Peltokangas M., Montero K. M., Honkanen M., Siponkoski T., Juuti J., Tuukkanen S., Oksala N., Vehkaoja A. and Mäntysalo M.

IEEE Sensors Journal, Accepted for publication 13.8.2019
(DOI 10.1109/JSEN.2019.2934943)